Marius Thorvik

Jamming-flow transitions of confined self-propelled rods

Masteroppgave

NTNU
Kunnskap for en bedre verden

Marius Thorvik

Jamming-flow transitions of confined self-propelled rods

NTNU

Kunnskap for en bedre verden

Jamming-flow transitions of confined self-propelled rods

Marius Thorvik

Trondheim, June 2021

Abstract

This thesis presents a computational investigation into the properties of a hybrid model of self-propelled rod-like particles in 2D interacting via apolar alignment and soft repulsion. So-called active particles represent a field of combined effort from statistical physics and biology, and the model intends to combine aspects of several previously studied models.

The simulated rods are modelled as straight continuous line segments surrounded by a soft repulsive potential, leading to overdamped collisions and allowing for dense clustering. Large ensembles of rods are simulated for long time intervals and various parameter values to determine their associated steady states with periodic boundary conditions and in a smooth channel.

Our simulations show a significant difference in qualitative behavior between systems with varying rod anisotropies. Our results correlate well with earlier studies conducted with periodic boundary conditions, but suggest different phase behavior when confined to the channel. Notable observations include the formation of a highly ordered boundary layer for short rods and the possibility of stable segregated lane formation at subcritical densities for long rods. The nature of the phase transition between these flow regimes may have applications in understanding the self-sustained transport of microbial suspensions in confinement.

Sammendrag

Denne oppgaven presenterer en numerisk undersøkelse av egenskapene til en hybridmodell av selvdrevne stav-aktige partikler i 2D som vekselvirker via apolar vinkeltilpasning og myk frastøtning. Såkalte aktive partikler representerer et kombinert fagfelt innen statistisk fysikk og biologi, og modellen er tiltenkt å kombinere aspekter fra flere tidligere studerte modeller.

Stavene som blir simulert er modellerte som rette og kontinuerlige linestykker omringet av et mykt frastøtende potensial, som frembringer overdampede vekselvirkninger gjennom kollisjoner, samt formasjon av tette klynger. Store ensembler av staver blir simulert over lange tidsintervaller og med forskjellige parameterverdier for å fastslå de tilhørende likevektstilstandene i periodiske grensebetingelser og i en glatt kanal.

Våre simuleringer viser en betydelig forskjell i kvalitativ oppførsel mellom systemer med ulik stav-anisotropi. Resultatene korrelerer godt med tidligere studier utført med periodiske grensebetingelser, men antyder forskjellige faseoppførsler ved innesperring i kanalen. Merkverdige observasjoner inkluderer formasjon av sterkt ordnede grenselag for korte staver, samt muligheten for formasjon av stabile separerte hastighetsfelt for lange staver ved subkritiske tettheter. Faseovergangens art kan bistå i vår forståelse av den selvdrevne transporten av mikroorganismer ved innesperring.

Contents

Preface

This thesis presents the work done for my M.Sc. degree in Applied Physics in the spring of 2021 at the Norwegian University of Science and Technology (NTNU). It builds upon my earlier work in computer simulations of active matter, a field of research I entered with no previous knowledge or experience, but for which I gained a lot of fascination while working on this project.

The previous work done for my specialization project last semester was focused on investigating systems of isotropic active particles and studying their jamming properties in the high-density regime. While resources related to the theory is starting to become abundant, the practical aspects of simulating these systems efficiently and accurately was a major challenge. Working towards overcoming these problems gave me a significant amount of insight and experience in developing, optimizing and testing large software projects, a process I very much enjoyed and have applied to the work done for my final thesis.

I would like to thank my supervisor Paul Gunnar Dommersnes for allowing me to write this master's thesis and for a lot of great guidance through frequent video meetings this past year. I also want to thank my family and friends both at home and in Trondheim who supported me though a time which was often difficult and stressful. This work has in every way been a collaborative project, and I am very grateful to everybody who encouraged me throughout my studies at NTNU.

Chapter 1

Introduction

1.1 The mesoscopic scale

A lot of the matter that surrounds us does not possess the properties we normally encounter in graduate-level physics. The field of solid state physics mainly deals with precisely uniform crystalline solids, objects with long-range spatial order. On the other end of the scale, fluid mechanics and statistical physics consider matter made entirely of randomly structured liquids and gases. In the area linking these fields, we encounter condensed matter systems which have gained much attention among researchers as well as in industry. The term *soft matter* is used to describe many of these systems, and are characterized by a asymmetries which generate mechanical interactions at the microscale and manifest through interesting dynamics in the intermediate mesoscopic scale. These dynamics further influence order and structure into the macroscale. Within the definition of soft matter we find polymers, granular colloids and quite importantly, liquid crystals [1].

Physical matter might exist in various phases which exhibit different properties. We can separate these phases by characterizing them through a number of order parameters: variables which quantify these properties and lets us make a comparative analysis of their behavior. In general microscopic descriptions, order is statistically controlled by the balance of entropy and stabilizing molecular interactions. In the areas where this balance goes through drastic changes, we observe phase transitions, either continuously or discontinuously. Discontinuous phase transitions are characterized by large order parameter fluctuations. Molecular interactions characteristically reside in the microscopic domain, while the order parameters can only be evaluated from the behavior of large condensed systems at the meso- and macroscale.

1.2 Active matter

1.2.1 Definition

In many ways, *active matter* encompasses an intersection of molecular dynamics and biology. Most of the matter surrounding our everyday lives is *passive*, or *thermal* - it naturally tends to reach a state of minimum free energy through random thermodynamic processes. Of course, passive does not mean stationary and non-changing. Systems may be *driven* out of thermodynamic equilibrium, be it by boundary conditions, mechanical perturbations or electric, chemical or other external gradients [2]. The processes that govern the behavior of such matter, as well as the corresponding probability theory is well understood by statistical mechanics. In active systems, however, the constituent particles characteristically drive the system from equilibrium internally by converting an infinite ambient energy source into self-propelled motion [3].

Canonical examples of living active matter include bacterial colonies and flocks of birds. Of course, neither of these are in actual conflict with the laws of thermodynamics. However, striking similarities in their collective motion across length scales sparked interest among physicists in the late 20th century. This lead to the emergence of multiple minimal models of synthetic active matter derived from simple components such as directed self-propulsion and local alignment mechanisms. These irreversible process leads to the breaking of time reversal symmetry, and thus thermodynamic equilibrium.

(a) (b)
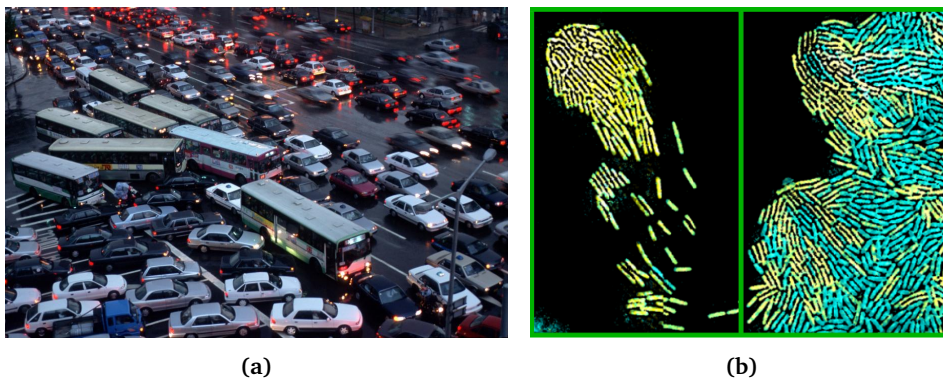
Figure 1.1: *Active matter*: Self-propelled agents come in various shapes and sizes. **(a)**: Traffic jam in Seoul, South Korea. Image by Martin Sasse[1]. **(b)**: Highly magnified image of a subsurface colony of *Pseudomonas aeruginosa*, with a portion (yellow) being a faster-moving genetically modified variant, showing separation and collective motion of clusters. Image reused from [4].

---

[1]https://www.nrc.nl/nieuws/2006/09/06/auto-uit-korea-wordt-te-duur-11188762-a420907

Active matter is composed of large numbers of *active particles*, a derivative concept from the more abstract active *agent*. An agent takes its conceptual origin from living beings, and generally describes a self-contained process that encapsulates some state and changes this state through proactive and reactive interactions with its environment and other agents. Large collections of agents realize a type of so-called *complex systems*, a name earned due to the inability to easily deduce their macroscopic behavior from the well-defined microscopic processes of the agents [5]. Due to the advent of powerful computers, agent-based modelling has in recent decades become a useful tool applied in both technology, economics and information theory. For the purposes of the work presented here, we specifically focus on classes of agents which do not deny their origin in the physical world, and will refer to them simply as active *particles* for now.

The active particles contain some set of external and internal variables. In addition to the generic properties of self-propulsion, agents may interact with the system through other specified rules. These interactions range from repulsive and attractive forces to particle birth and death. Different rules may generate different large-scale effects, such as cooperative or competitive behavior. From large multiagent systems we may observe the emergence of collective motion [6], agent ecology and evolution [5], and to the formation of structures much larger than the individual agents, such as topological defects [7]. The range of possible interactions and boundary conditions are limitless, and active matter is a field still being explored in a unified effort by both physicists and biologists.
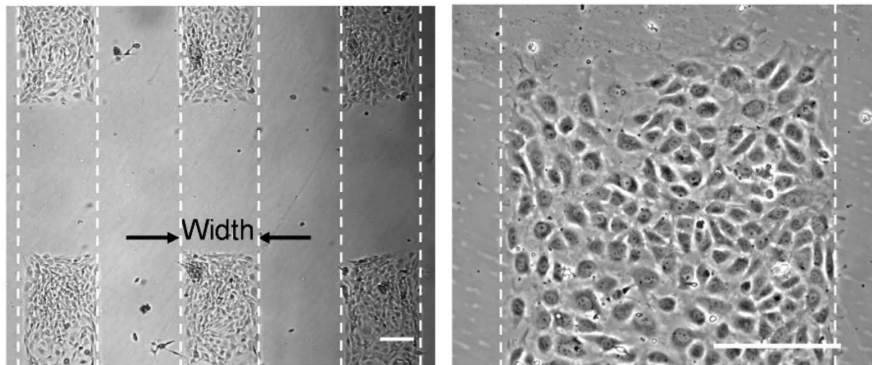
Figure 1.2: *Confined system*: Magnified images of human endothelial cells confined to a narrow channel. The collective migration of these cells are important to the maintenance of the tissue lining the inner part of blood vessels. Adapted from [8].

1.2.2 Active phase transitions

Since its conception, theoretical and experimental work on multiagent active systems has spanned a large spectrum of sizes and complexities, from traffic flows [9] to human crowds during mass events [10]. The main inspiration and most notable application has been related to the study of coherently moving flocks of animals and collections of cells [11]. Their physical commonality as active matter allows us to make general statements about their dynamics. In addition to exhibiting interesting behavior at a large scale, varying the microscopic properties of the system leads to new types of active phase transitions. The properties that drive some of these transitions are still not fully understood, as opposed to the case of most passive matter.

As a contribution, we conduct an investigation of how different microscopic interactions and boundary conditions influence certain phase transitions. This thesis will examine the properties of active particles confined to simple geometries, and more specifically try to determine how *particle shape* affects the observed phase behavior and the transitions between them. Dense collections of active particles confined to special geometries are relevant to a wide range of contexts. As an example, human cells within biological channels (e.g. blood vessels) have been studied in order to determine the physics of tissue repair (see Figure 1.2). To study the non-trivial physical phenomena that arise in active matter systems, we first outline the components and implementation of common theoretical active matter models. We later define a suitable model of elongated active rods with which we perform discrete element simulations.

The remaining chapters of this thesis will present the following:

- Chapter 2 motivates and gives an introduction to computational active matter models and the theory related to their most important elements.
- Chapter 3 describes the practical considerations for the implementations of these models.
- Chapter 4 presents results from simulations performed for systems with chosen parameters and boundary conditions, as well as some statistical theory related to the results.
- Chapter 5 summarizes the main conclusions to the problems in question, and presents a discussion of the employed methodology.

Chapter 2

Models

2.1 Motivation

Even simple models are able to describe complex features of reality. As an example, the Ising model of quantum spin ensembles is a simple, but revolutionary model which can be made more complex step-by-step. The initial task of reducing an observed phenomenon to its most basic components lets us consider each one in order, making it easier to understand the whole picture.

Research, both theoretical and experimental within the field of active matter can be complicated in the most simple situations. Setting up well-controlled experiments on physical systems is difficult, as the number of influencing factors may be hard to evaluate and control independently. In the case of microbiological systems such as cells, the presence of external chemical gradients and genetic factors are examples of issues with potentially large effects [12]. These necessitate good descriptions in-and-of-themselves for observations to be useful. Experimental work therefore often makes use of man-made micro- or nanoscopic objects with known properties and parameters, such as vibrated granular materials. For complete control, however, physical systems are replaced entirely by numerical experiments. The advantages of this approach are numerous: Simulations can be made as complex as one wishes and results may also be quickly produced and directly compared to theory. The immense increase in power and accessibility of computers has lead this being a highly relevant approach.

Areas concerned with complex systems such as molecular dynamics may make great use of our increasingly fast and affordable computers, in addition to the possibility of parallelization. Molecular dynamics requires that we keep track of both positions and trajectories of particles. For simulations of condensed matter in equilibrium, it is thus computationally more costly than methods based on the thermodynamic averages, such as Monte Carlo methods [13]. Both are similar in that molecules are treated as classically interacting particles, but differ in how particles are moved about in time. For non-equilibrium simulations, particle- or *agent-based* simulations are required when we want a detailed description of microscopic features [5], due to the difficulty of matching these to an analytic model.

In terms of implementation, we want to compute equations of motion at the level of each particle. We aim to study systems of suspended colloids where the density and short-range interactions may induce phase separations that are impossible to achieve in continuum models. These include the *motility-induced phase separation* and *jamming* transitions observed in the presence of self-propulsion and short-range repulsion. The discrete particle model allows us to control each element of the interactions and measure microscopic details of the states, giving a realistic picture with easily interpreted physical features.

2.2 Classifying active particles
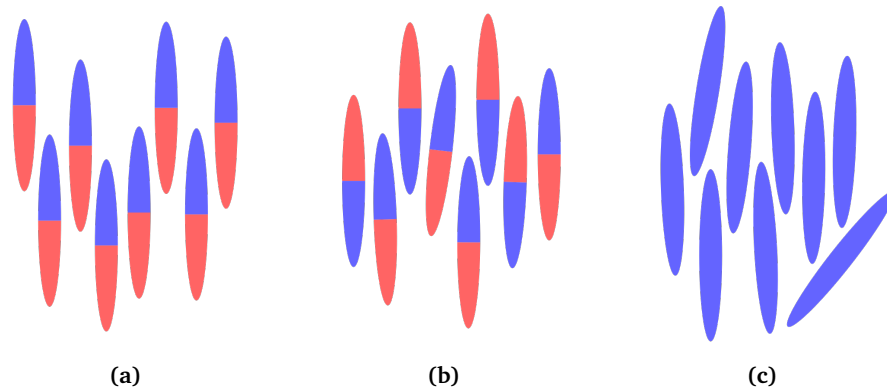
2.2.1 Symmetry and polarity

A large part of the interest surrounding active matter is how non-equilibrium interactions may cause spontaneous self-organization of the systems. Going into the microscopic details of how these interactions work can help us understand how they drive these phase transitions. The primary questions is how the particles themselves are structured. If particles are imagined as isotropic spheres in space, we would naturally not expect the flocking behavior we see in groups of living creatures. Anisotropies, such as complex shapes and directional interactions can drive symmetry breaking and induce ordering [14]. In 2D space, we generally consider three typical ordering schemes: Ferromagnetic-like ordering of *polar* particles with a distinct front and rear, where all the particles on average are pointing in a fixed direction; *Nematic* ordering, seen in particles with an elongated uniaxial symmetry; No orientational ordering, when particles are effectively circular in shape [14]. The different ordered states do not, however, uniquely correspond to each symmetry of particle pair interactions. Polar particles subject to extremely short-range interactions may enter a dense stable nematic phase when constrained by crowding [3] (see Figure 2.1). Likewise, strictly apolar interactions can result in the formation of polar clusters of aligned particles due to activity-induced separation. To make the distinction of these interactions clearer, we will discuss these symmetries in detail.

2.2.2 Polar interactions

Polar particles are characterized by a distinct head-tail symmetry which defines their orientation in space and in relation to other particles. For active particles, this orientation generally defines their direction of self-propulsion and acts as the principal mechanism of intermolecular interactions. The latter property is of significant importance due to spontaneous breaking of rotational symmetry, leading to large-scale systematic behavior in conjunction with active motion. The type of intrinsic polarity assumed for this type of matter is often a simplified analogy of biological processes, such as distinguishable "heads" (usually containing long-range sensory organs) and "tails". In 2D, examples include herds of sheep con-

fined to the surface of the Earth, and in 3D, a flock of birds. Polar interactions can span a wide range of length and time scales. Ferromagnetic organization of polar particles imitates the interaction of magnetic dipoles, where large-scale organization stems from dipoles aligning with their neighbors to minimize energy. In the case of non-equilibrium systems, the same self-organization have been shown in *in vitro* studies of kinesin, a motor protein which moves along polar microtubules from hydrolysis of ATP [15].

(a) **(b)** **(c)**

Figure 2.1: *Polarity and ordering*: Primary ordering schemes of particles with different symmetry: **(a)**: Polar ordering of polar particles, **(b)**: Apolar (nematic) ordering of polar particles, **(c)**: Nematic ordering of apolar particles.

2.2.3 Active nematics

Nematic particles, or *nematics*, comprise a class of particles with properties distinctly different from particles with polar interactions. Their characteristic properties are closely associated with those of liquid crystals, which are composed of symmetric, elongated molecules. Dense liquid crystals lack the regular structure of solid crystals. Constituent atoms in crystals typically organize in periodic structures, forming solid bulks of robust matter. Nematics, on the other hand, form *amorphous* or *glassy* solids at a critical temperature and density. Research into colloidal nematic liquid crystals is plentiful, largely due to the popularity of liquid crystal displays in modern electronics [16].

Nematic particles naturally interact via apolar interactions, leading to passive alignment. The macroscopic ordering has an $\mathbf{n} = -\mathbf{n}$ invariance of its mean orientation. Non-equilibrium nematics can generate large number fluctuations similar to polar systems through contextual active stresses, such as pushing or pulling against other particles or the environment [17]. The nematically ordered phase has major relevancy to the dynamics of dense collections of cells. Migrating cells may spontaneously move in "streams" during embryonic development or cancer metastasis. This is usually attributed to cell-cell adhesions, but cells lacking stable adhesions have been shown to order into a nematic phase and moving collectively as a consequence [18].

2.3   The Vicsek model

The Vicsek model, proposed in 1995 by T. Vicsek et al. [19], is an algorithm originating in the early effort to mimic the non-equilibrium behavior of biological systems. More specifically, the model intends to demonstrate the emergent phase transitions of a system of self-propelled particles with polar ordering. The model considers a system of N point particles in an $L \times L$ continuous 2D space with periodic boundary conditions to emulate an infinite system. Each particle's absolute velocity v is kept constant, making their individual orientation with respect to the x-axis, θ_i, the only parameter of their motion in the plane. The rule of the Vicsek model is as follows: At each time step, the orientation of each particle is updated to equal the average orientation of the particles in its neighborhood of radius R, in addition to some random noise. A particle i described by its position $\mathbf{r}_i$ and velocity $\mathbf{v}_i = v\hat{\mathbf{x}}\cos\theta_i + v\hat{\mathbf{y}}\sin\theta_i$ moves in the plane by an Euler-step

$$\mathbf{r}_i(t + \Delta t) \, = \, \mathbf{r}_i(t) + \mathbf{v}_i(t)\Delta t \tag{2.1}$$

$$= \, \mathbf{r}_i(t) + v\Delta t\hat{\mathbf{x}}\cos\theta_i(t) + v\Delta t\hat{\mathbf{y}}\sin\theta_i(t) \tag{2.2}$$

and the particle's direction of motion θ_i is calculated by

$$\theta_i(t + \Delta t) = \langle \theta_j(t) \rangle_{|\mathbf{r}_j - \mathbf{r}_i| \leq R} + \Delta\theta_i. \tag{2.3}$$

The noise term $\Delta\theta_i$ is generated from a uniform random probability distribution $\Delta\theta_i \in [-\eta/2, \eta/2]$, and represents an effective system *temperature*. The term temperature is not strictly applicable to this type of non-equilibrium system; it is only an intuitive interpretation of *rotational diffusion*. As this term corresponds to a certain added angle, η is more intuitively represented as a multiple of π radians, and its value range is effectively restricted to $\eta = [0, 2\pi]$ due to periodicity. In the most extreme case, $\eta = 2\pi$, the particle may occasionally make a complete reorientation regardless of the state of its neighborhood, making the orientation θ_i completely uncorrelated in time. Some trigonometry is required to obtain the averaged orientation $\langle \theta_j(t) \rangle$, which must be computed component-wise on the unit circle. A visual summary of the Vicsek model is shown in Figure 2.2.

To quantify the phase transition of the system we will use the global average velocity of the particles in the system as a general order parameter [19]

$$v_{\mathrm{a}} = \frac{1}{N}\left|\sum_{i=1}^{N}\mathbf{v}_i\right|. \tag{2.4}$$

A completely scrambled system with uniformly distributed orientations will correspond to a minimum value of $v_{\mathrm{a}} = 0$. Conversely, for an almost completely coherently moving system, $v_{\mathrm{a}} \approx 1$. In the case that the particles are considered passive, $v = 0$, the Vicsek model is identical to the 2D ferromagnetic Ising model, where
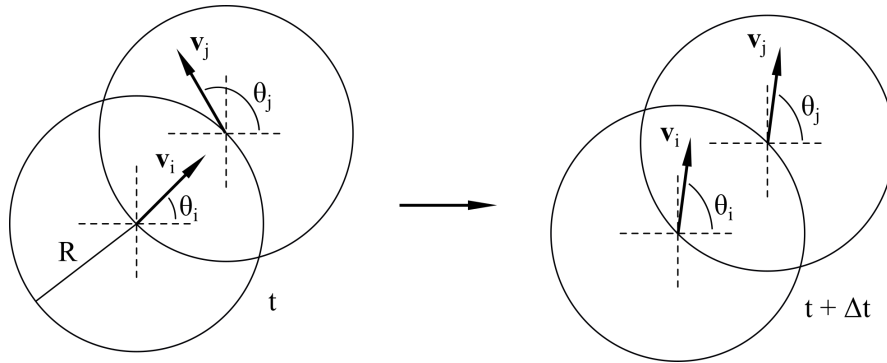
Figure 2.2: *Vicsek model*: A particle calculates its new angle θ from the average of its neighbors within $|\mathbf{r}_j - \mathbf{r}_i| \leq R$, in addition to a noise term.

a random distribution of particle "spins" corresponds to a high-energy configuration of the system. These spins experience short-range interactions which depend only on their relative orientations, and these interactions tend to align them to their neighbors to minimize energy. Thermal forces also have an influence, and similarly determine the equilibrium state of the system, where a zero-temperature limit will correspond to a perfectly magnetized state at $t \rightarrow \infty$.

2.3.1 Simulations and results

In order to compare the simple Vicsek model with the more complex methods used later, some simulations were run to see how some key properties of active matter spring out from the models. These simulations do not constitute a rigorous analysis of the model, we only want to make qualitative statements about the properties of the model[1].

Four separate simulations based on the Vicsek algorithm were carried out with a particle number $N = 1024$ and system size $L = \sqrt{N} = 32$ with periodic boundary conditions, resulting in particle number density $\rho = 1$. Noise parameters were chosen to somewhat evenly sample the spectrum of possible values, including the infinite-temperature limit $\eta = 2\pi$. The particle interaction radius was set to $R = 1$; the time step length was set to $\Delta t = 10^{-2}$ and the active particle velocity to $v = 5$. The length of the simulation was chosen to allow the system to reach a steady state, and a total time of $t_{\max} = 6 \cdot 10^3 \Delta t$ was determined to be sufficient. Figure 2.3 shows the measurements of the average velocity of the particles in the system v_a as a function of running time t. Snapshots of the final states are shown in Figure 2.4, giving a visual representation of how the noise affects the system steady state.

---

[1]Note: The results in this section stem from simulations performed for my specialization project. The data is thus of worse quality, but illustrate the behavior of simple active matter models.
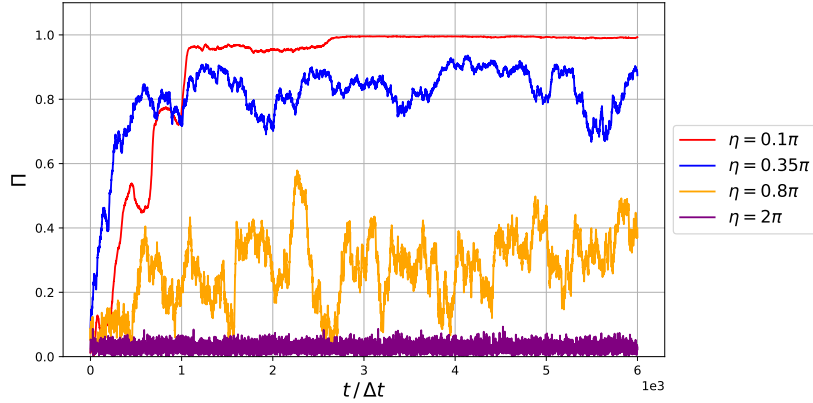
Figure 2.3: *Order evolution*: Average velocity v_a over time for four different values of the noise intensity η. $v = 5$, $N = 1024$, $\rho = 1$. The transitional noise regime between almost complete order for $\eta = 0.1\pi$ and a disordered state for $\eta = 2\pi$ shows large order fluctuations around an apparent critical temperature.

2.3.2   Discussion

The evolution of the order parameter v_a shown in Figure 2.3 gives some good insight into how the effective temperature of the system influences the transient and steady state properties of the Vicsek systems. The system with $\eta = 0.1\pi$ shows the highest and most stable order, and is even at certain points at almost perfect order. This makes sense, as less noise would make it easier for particles to stick together once they are within the alignment radius R. However, since the noise is nonzero, small clusters of particles occasionally split off and later recombine with the main particle cluster within a short time. The total order thus remains stable after the initial mass flocking of the system.

Systems with higher noise amplitudes are characterized by a decreasing cohesion and lower total order as a result. An interesting observation from 2.3 is that while all four systems are initiated in complete disorder, systems of higher noise amplitudes seem to reach their steady state quicker than the less noisy systems. This may be due to larger diffusive behavior in the particles, effectively increasing their neighborhood of influence and causing quicker flocking, a point deemed plausible by Vicsek himself [19]. As expected, for the system of infinite effective temperature, $\eta = 2\pi$, the system maintains extremely high disorder and experiences small fluctuations. The particles are practically unable to align themselves to each other, as the reorientation is dominated by the noise.

In the noise regime between the two extreme states, the evolution of v_a is characterized by large fluctuations. These fluctuations were predicted to be due to a phase transition located at a critical effective temperature point. It was later shown that the phase transition is in fact discontinuous [20]. The Vicsek model demonstrates the descriptive ability of simple active matter models, and motivated the development of more realistic models.

(a) $\eta = 0.1\pi$. Highly ordered phase.

(b) $\eta = 0.35\pi$.

(c) $\eta = 0.8\pi$.

(d) $\eta = 2\pi$. Isotropic phase.

(e)
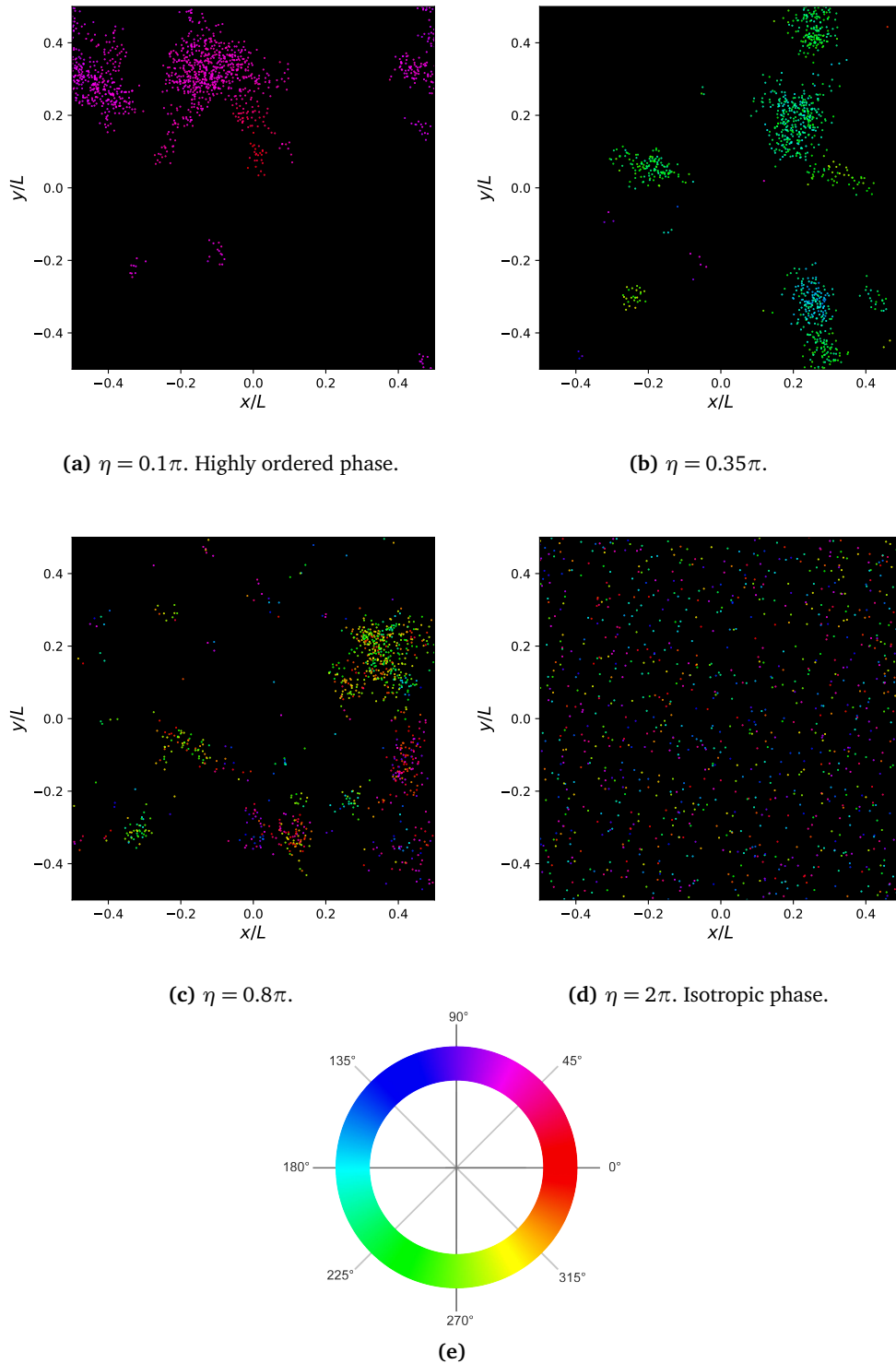
Figure 2.4: *Ordering of aligning particles*: **(a-d)**: Snapshots of the final states of active systems run with the Vicsek algorithm and different values for the noise parameter η. $N = 1024$. Colors indicate orientation θ_i, mapped to **(e)**.

2.4   Brownian particles

In the introductory chapter, we defined the concept of an active agent and later made observations from the simple, yet informative Vicsek model of active point particles. We will now expand on the simplistic model and combine it with the concept of a *Brownian agent*. In order to manifest more realistic behaviors in our simulations of active systems, we need to model dynamics at more general time and length scales. In the field of molecular dynamics, Brownian particles are oftentimes used as a reductionist model of the deterministic and stochastic processes which drive the dynamics of particles at the microscale. Likewise, Brownian agent models are used to represent a relatively simplistic form of agent for which one can define a set of microscopic rules to excite large-scale behavior [5]. Observing the emergent properties of the system rather than complex individual behavior will allow for more general interpretations and applications of our model. Additionally, observing the system at this mesoscopic level allows us to investigate the nature of the emergent phases of the system.

2.4.1   Passive Brownian particles

As an initial generalization of the Vicsek model, we consider the Newtonian ansatz for an isotropic disk i with mass m centered in $\mathbf{r}_i = \mathbf{r}_i(t)$ with orientation θ_i:

$$m\ddot{\mathbf{r}}_i = \mathbf{F}_{\text{ext}} + \mathbf{F}_{\text{drag}} + \mathbf{F}_{\text{stoch}}, \tag{2.5}$$

where $\mathbf{F}_{\text{ext}}$ comprises any external (center-of-mass) forces, $\mathbf{F}_{\text{drag}} = -\gamma_t m\dot{\mathbf{r}}_i$ describes a dissipative friction force and $\mathbf{F}_{\text{stoch}}$ is a time-dependent stochastic noise term from random collisions between the disk and the momentum-absorbing solvent medium [5]. From the fluctuation-dissipation theorem, the friction of the medium and stochastic forces vanish on average, and we can write $\mathbf{F}_{\text{stoch}}$ as a force with zero mean, strength $D_t = k_B T / \gamma_t$ and δ-correlated time dependence. Equation 2.5 then becomes [5]

$$m\ddot{\mathbf{r}}_i = \mathbf{F}_{\text{ext}} - \gamma_t \dot{\mathbf{r}}_i + \gamma_t \sqrt{2D_t}\, \boldsymbol{\eta}_i(t) \tag{2.6}$$

$$\langle \boldsymbol{\eta}_i(t) \rangle = \mathbf{0}, \quad \langle \boldsymbol{\eta}_i(t) \cdot \boldsymbol{\eta}_j(t') \rangle = \delta_{ij}\, \delta(t - t'),$$

describing a random diffusive walk, so-called *Brownian motion*. Although this walk conserves orientation, the particle simultaneously experiences a rotational force governed by rotational friction with the solvent medium, given by

$$I\ddot{\theta}_i = M_{\text{drag}} = -\gamma_r \dot{\theta}_i, \tag{2.7}$$

We are mostly interested in the case where the friction terms containing γ_t, γ_r completely cancel the forces at any point in time, leading to no net acceleration of the system in time. This is justified by the fact that microscopic particles typically

reside in the low-Reynolds-number regime [21], where viscous forces dominate over inertial forces. In this overdamped approximation, we get

$$\gamma_\mathrm{t}\dot{\mathbf{r}}_i = \mathbf{F}_\mathrm{ext} + \gamma_\mathrm{t}\sqrt{2D_\mathrm{t}}\,\boldsymbol{\eta} \tag{2.8}$$

$$\gamma_\mathrm{r}\dot{\theta}_i = 0, \tag{2.9}$$

commonly called the overdamped Langevin equations, in attribution of Paul Langevin [22]. This defines the dynamics of a *passive Brownian particle* (PBP), where the motion of the particle is determined by external forces and some random noise, leading to purely diffusive behavior in the case that $\mathbf{F}_\mathrm{ext} = 0$.

2.4.2 Active Brownian Particles

Continuing on the equations for passive Brownian particles, we include the mechanics that move these dynamics from the realm of equilibrium physics into one of non-equilibrium. We impose a constant self-propulsion force on each particle, where the energy to drive the propulsion is supplied continuously and irreversibly to counteract friction. The self-driving force $\mathbf{F}_\mathrm{p}$ acts along the particle's polarity, propelling it at a velocity $v_\mathrm{p}\mathbf{e}_i = v_\mathrm{p}(\hat{\mathbf{x}}\cos\theta_i + \hat{\mathbf{y}}\sin\theta_i)$, where $v_\mathrm{p} = F_\mathrm{p}/\gamma_\mathrm{t}$.

By including the self-driving force, the new system of *active Brownian particles* (ABPs) is characterized by the particle density ρ and temperature D_t in addition to two new control parameters, namely the persistence time of the active force and its strength [2]. The particles will move along their long axis and experience small random perturbations as they move. We can assume that in most cases, the constant driving velocity v_p will significantly dominate the diffusion of the thermal noise [23]. In order to preserve the diffusive behavior of the Brownian particle, we move the stochastic noise term from the translational equation and into the rotational one, creating a *persistent random walk* similar to the Vicsek model. By neglecting the translational effects of temperature, we simplify the parameter space and now control the persistence time of the particle's motion through the rotational diffusion coefficient D_r.

We expand $\mathbf{F}_\mathrm{ext}$ to only include a lateral pairwise force acting in the particle's center-of-mass from other ABPs in the system. From this point we also add to our model that the ABPs may gain rotational energy M_{ij} from some similar torque-like interaction. If neither of these interactions pertain to solvent-mediated hydrodynamic effects caused by flows from particle motion, this characterizes *dry active matter* [3], systems without momentum conservation. We are then left with the updated equations

$$\dot{\mathbf{r}}_i = \frac{1}{\gamma_\mathrm{t}}\sum_{j\neq i}^{N}\mathbf{F}_{ij} + v_\mathrm{p}\mathbf{e}_i \tag{2.10}$$

$$\dot{\theta}_i = \frac{1}{\gamma_\mathrm{r}} \sum_{j \neq i}^{N} M_{ij} + \sqrt{2D_\mathrm{r}}\,\xi \tag{2.11}$$

$$\langle \xi_i(t) \rangle = 0, \quad \langle \xi_i(t)\xi_j(t') \rangle = \delta_{ij}\,\delta(t - t'). \tag{2.12}$$

In 2D and 3D, the gradual reorientation of such ABPs has been shown to be equivalent with another class of active particle models, so-called *run-and-tumble particles* (RTP), where the particle moves persistently and occasionally reorients by Poisson-distributed "tumbles". This swimming strategy is observed in the motion of common bacteria, such as *E. coli* [24]. In cases where the motility parameters are independent of $\mathbf{e}_i$, the random-walk with diffusivity D_r can be seen as a continuous equivalent of the sudden reorientations of RTPs [25], despite their difference in the short-time dynamics.

2.4.3 Repulsive forces

With the equations of motion of the individual ABPs laid out, we turn our focus to the details of the interactions between particle pairs. In the Vicsek model, this interaction was limited to systematically conform the orientations of particles to neighbors within a specified region. This rule does not, however, restrict the possible positions of particles within the system. Local particle densities may then grow arbitrarily large, leading to difficulty in making statements about the size of the system.

If we assume that particles are impenetrable objects of finite size, we can implement a passive area exclusion interaction, a so-called *steric interaction* [6]. For circular particles of radius R, the simplest and most intuitive solution is to enforce a rule of some maximal interparticle distance $\sigma = 2R$. We interpret this as a discontinuous infinite potential barrier surrounding each point-particle, exerting a force in each particle's center-of-mass. This *hard-center* model is unsuited for numerics with finite time steps, as this potential will abruptly exert an infinite force on particles for center-to-center distances $r < \sigma$. To mitigate this issue, we instead use a soft continuous potential with a finite gradient that is more repulsive the closer the particles are to each other. The force is thus reduced to a more practical size for the simulations. Additionally, as we will discover in the consideration of particle shape, this center-of-mass separation mechanism may be simultaneously used to determine rotational interactions. It also impacts system parameters such as density. The details of this mechanism is therefore important to the dynamics of the system, necessitating deliberation when choosing the appropriate model.

Examples of soft passive interaction include a spring model [26], where the repulsion is modelled by a spring pulling the particles normally away from each other, and exponential potentials such as the Yukawa potential [27]. Perhaps the most extensively used model for a realistic intermolecular potential is the *Lennard-Jones potential* [28]. In the original formulation of the Lennard-Jones potential

(commonly called the *12-6-potential*), the magnitude of the potential for two particles with a center-to-center distance r is given by

$$U_{\mathrm{LJ}}(r) = 4\epsilon \left[\left(\frac{\sigma}{r} \right)^{12} - \left(\frac{\sigma}{r} \right)^{6} \right]. \qquad (2.13)$$

Here, σ denotes the effective diameter of each particle in the dimensions of length, and ϵ has dimensions of energy [29]. The potential is zero for $r = \sigma$, separating two regions of attraction and repulsion for $r > \sigma$ and $r < \sigma$, respectively. The short-range r^{-12} part describes repulsion due to the Pauli exclusion principle, and the r^{-6} part is an attractive term inspired by induced electrostatic forces. As we are only interested in the repulsive part of this potential, we split it at its minimum $U(r_{\mathrm{min}}) = -\epsilon$, raise the minimum value to $U(r_{\mathrm{min}})$ and enforce $U(r) = 0$ for $r > r_{\mathrm{min}}$. This new truncated potential is commonly called the *Weeks-Chandler-Andersen* (WCA) potential [30]

$$U_{\mathrm{WCA}}(r) = \begin{cases} 4\epsilon \left[\left(\frac{\sigma}{r} \right)^{12} - \left(\frac{\sigma}{r} \right)^{6} \right] + \epsilon, & r \leq r_0 \\ 0, & r > r_0. \end{cases} \qquad (2.14)$$

For the simulations in this work, high densities might lead to large forces if a particle experiences forces from many directions. The r^{-12}-term acts quite quickly, which comes with a rather large risk of causing numerical issues. As a preventative solution, reducing the exponents from 12-6 to 6-3 drastically reduces this risk. Because the 12-6 exponents are somewhat arbitrary, we are free to choose the softer potential as long as we can define an effective size of the particles. The 6-3 modified WCA-potential becomes

$$U_{\mathrm{rep}}(r) = \begin{cases} 4\epsilon \left[\left(\frac{\sigma}{r} \right)^{6} - \left(\frac{\sigma}{r} \right)^{3} \right] + \epsilon, & r \leq r_0 \\ 0, & r > r_0. \end{cases} \qquad (2.15)$$

The force acting on a particle within this potential along the center-to-center direction $\mathbf{r}$ is then given by the derivative $\mathbf{F}_{\mathrm{rep}}(r) = -\partial_r U_{\mathrm{rep}}(r)\hat{\mathbf{r}}$:

$$\mathbf{F}_{\mathrm{rep}}(r) = \begin{cases} 4\epsilon \left[\frac{6}{r} \left(\frac{\sigma}{r} \right)^{6} - \frac{3}{r} \left(\frac{\sigma}{r} \right)^{3} \right] \hat{\mathbf{r}}, & r \leq r_0 \\ \mathbf{0}, & r > r_0. \end{cases} \qquad (2.16)$$

Solving for $F_{\mathrm{rep}}(r) = -\partial_r U_{\mathrm{rep}}(r) = 0$ gives a value of $r_0 = 2^{1/3}\sigma \approx 1.26\sigma$, the *cut-off radius* for the modified WCA-potential, where the repulsive forces become non-zero. By this transformation, what we called the effective diameter σ is now the point at which the potential is $U = \epsilon$. With the truncated WCA-potential, r_0 can thus be regarded as the new "de facto" diameter of the soft particles. The original Lennard-Jones potential and the modified WCA-potential are shown in Figure 2.5.

(a)

(b)
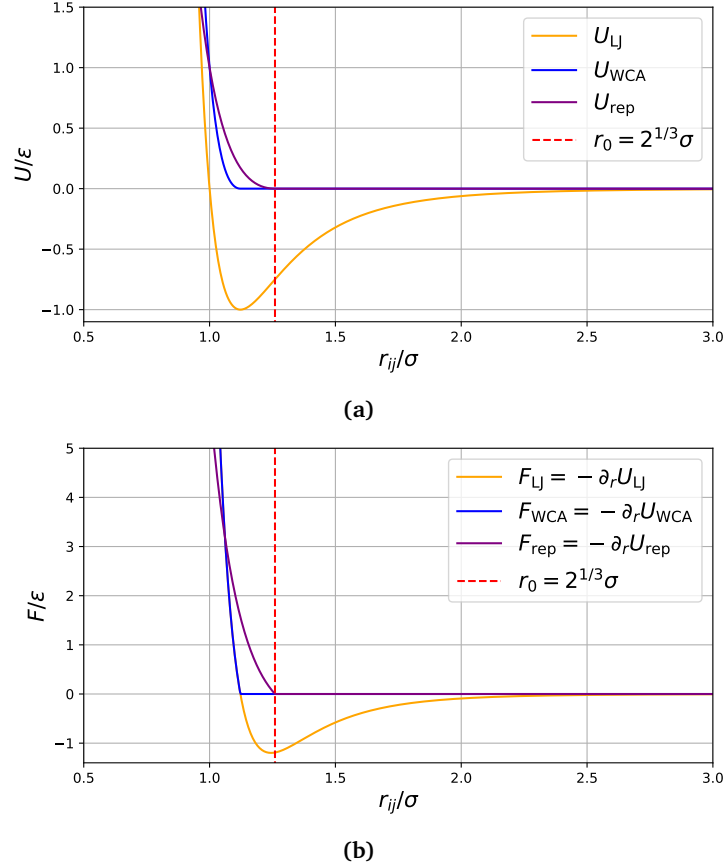
Figure 2.5: *Repulsive potential*: **(a)**: Original Lennard-Jones potential and the modified truncated WCA-potentials. By lifting the potential by ϵ, the $U = 0$-point is shifted from σ to r_0. **(b)**: Forces calculated from the radial derivatives of (a), showing the softer slope of the modified potential U_{rep}.

2.5 Active Brownian rods

2.5.1 Particle shape

As discussed in Section 2.2, the symmetries associated with the pairwise interactions are critical considerations which strongly influence how systems of particles evolve and behave mechanically. This is particularly significant in the high-density regime, where frequent collisions within clusters dominate the dynamics. If we narrow our focus to apolar grains, we still face an enormous range of possibility in terms of particle shape [31]. The shape we consider must ideally meet several criteria depending on the context of our model. If we require that the particles are effectively aspherical, as is typical in the study of active matter, we need a way of controlling the asphericity. Furthermore, any other anisotropies should be characterized by a minimal number of parameters to maintain a manageable amount of parameters.

Perhaps most importantly, the shape should allow for accurate and efficient calculations of contact distances between particles to determine the magnitude of distance-dependent forces. In both 2D and 3D, using ellipsoidal particles is a tempting option, due to their simple mathematical description. Calculating the contact distance between two ellipsoids in arbitrary configurations is, however, quite complicated [31]. Popular solutions to this issue involve approximating ellipsoids by constructing rigid polymers of multiple perfect spheres [32] or as smooth spherocylinders [33].

(a) (b)
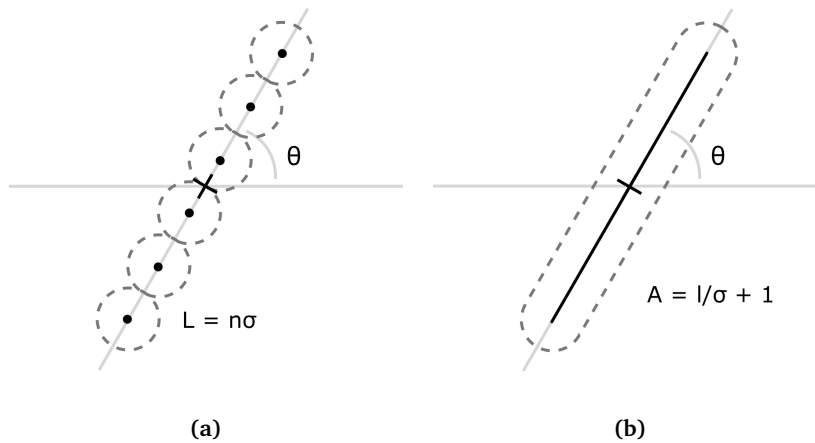
Figure 2.6: *Rod models*: Schematic representation of two prominent constructed rod models, the rigid n-mer rod **(a)** and the line segment rod **(b)**. Both may be used to approximate short ellipsoids and longer filaments, as well as allowing for simple collision calculations.

2.5.2 Linear rod model

Because we want to make our model as applicable as possible to the context of microbiology, we choose to consider a model of smooth anisotropic self-propelled rods. Previous studies have examined models of flexible rods, but due to the expanded parameter space, we will focus on rigid, linear rods. These are constructed from a straight line segment of length l surrounded by a repulsive potential with a cut-off diameter of length $r_0 = 2^{1/3}\sigma$. The continuous inner line segment lets us neglect friction from the varying rod thickness we might otherwise expect in models based on chains of discrete spheres. In the high-density regime, then, we can disregard effects caused by this somewhat unnatural geometry. Using σ as the effective rod width, the shape is characterized by the rod aspect ratio [33]

$$A = \frac{l}{\sigma} + 1. \tag{2.17}$$

The rods may thus approximate the shape of ellipsoids for small values of A and longer filaments for large A.

The dynamics of the rods will be based on the equations for ABPs. Due to the particles now being modelled as anisometric rods, the viscous friction coefficients of the forces parallel and perpendicular to the rod axis are no longer equal. For a straight rod with diameter σ and length $A\sigma$ dragged through a fluid with a force $\mathbf{F}$, the flow in the low-Reynolds number regime is given by the linear equation

$$\mathbf{F} = \boldsymbol{\gamma} \cdot \dot{\mathbf{r}} \tag{2.18}$$

In the long and slender-limit $A \to \infty$, the friction coefficient in the long axis direction is half as big as for movement normal to it [34]. In 2D, this yields the friction matrix

$$\boldsymbol{\gamma} = \begin{bmatrix} \gamma_\parallel & 0 \\ 0 & \gamma_\perp \end{bmatrix} = \begin{bmatrix} \gamma_\parallel & 0 \\ 0 & 2\gamma_\parallel \end{bmatrix}, \tag{2.19}$$

where $\gamma_\parallel = A\sigma\gamma_0$. The rotational friction coefficient is given by $\gamma_r = A^2\sigma^2\gamma_\parallel/6$ [33]. We now decompose the translational equation 2.10 to treat these axes of movement separately:

$$\dot{r}_{i,\parallel} = \frac{1}{\gamma_\parallel}\left[\sum_{j\neq i}^{N} F_{ij,\parallel} + F_{\mathrm{p}} \right] \tag{2.20}$$

$$\dot{r}_{i,\perp} = \frac{1}{\gamma_\perp} \sum_{j\neq i}^{N} F_{ij,\perp}, \tag{2.21}$$

and along with the rotational motion by equation 2.11, these three equations form the complete equations of motion for an individual *active Brownian rod* (ABR). The self-propulsion speed now takes the form $v_{\mathrm{p}} = F_{\mathrm{p}}/\gamma_\parallel$ and the collision-induced rotational energy term M_{ij} in equation 2.11 is defined by the cross-product

$$M_{ij} = \left[a(\mathbf{r}_i, \mathbf{r}_j; \theta_i, \theta_j)\,\mathbf{e}_i \times \mathbf{F}_{ij,\perp} \right] \cdot \hat{\mathbf{n}}. \tag{2.22}$$

Here, $a \in (-l/2, l/2)$ is the distance from the center-of-mass of rod i to the point where the force $F_{ij,\perp}$ from rod j is exerted and $\hat{\mathbf{n}}$ is the normal vector of the 2D plane. The method of calculating a, as well as an illustration of the forces involved, is shown Section 3.3.

In summary, the computational model outlined in this section defines the dynamics of an elongated apolar ABR characterized by its aspect ratio A. The state of the rod is given by its 2D center-of-mass position $\mathbf{r}_i$, its velocity $\dot{\mathbf{r}}_i$ and its polarity $\mathbf{e}_i = \hat{\mathbf{x}}\cos\theta_i + \hat{\mathbf{y}}\sin\theta_i$. It is internally driven by a force F_{p} along its polarity, while subject to rotational diffusion with strength D_{r}. During collisions with other rods, it experiences center-of-mass translational and rotational forces depending on the distance of contact, as well as the point and angle of incidence. The next chapter will present the method of model implementation and discuss the parameters associated with the numerical experiments.

Chapter 3

Simulating Active Brownian Rods

3.1 Computer implementation

The main suite of programs used to simulate our systems were implemented in C++, a high-level programming language compatible with object-oriented simulation. The agent-based approach of our active particle model is object-oriented by definition [5], making this an appropriate paradigm for practical implementation. As a compiled language, C++ is typically much faster compared to interpreted languages such as Python. The code is optimized further using multithread parallelization using the OpenMP extension. This allows simulations of a high number of particles to be performed on standard computer hardware with reasonable runtimes. Object-oriented simulation is a particularly suitable method for parallelized molecular dynamics computations, as the work load is organized in easily divisible chunks that are distributed across multiple processor nodes. Tasks contained in each chunk are performed in a serial manner, including the calculation of new variables and integrating the equations of motion, the details of which will be presented in a later section.

All the simulations for this thesis were performed on standard home computers, although creating a framework for running the software on external hardware would have allowed for major improvements in total runtime. In this case, an increased number of simultaneous simulations could have been conducted in order to gather better statistics overall. However, with optimizations in form of code parallelization and rewriting functions to more efficiently calculate quantities such as the intermolecular distance between rods, we could perform simulations of $N \simeq 2 \cdot 10^3$ for relatively long system-time intervals $t \sim 300\tau$ in about two hours of real runtime. Other optimization alternatives and information related to the practical implementation of the methods in this chapter is described in Appendix A.

3.2   Units and parameters

3.2.1   Persistence number

We start by considering the motion of a single rod obeying the ABR equations 2.20, 2.21 and 2.11. In the absence of other rods, we can neglect the transverse velocity, as F_{ij} represents an exclusively pairwise interaction. From the rotational noise term defined in equation 2.12, the orientational correlation function for the rod is given by [30]

$$\langle \mathbf{e}_i(t) \cdot \mathbf{e}_i(0) \rangle = e^{-t/\tau_{\mathrm{r}}} \tag{3.1}$$

where $\tau_{\mathrm{r}} = 1/D_{\mathrm{r}}$ is the *persistence time* of the particle's orientation, quantifying the average length of time θ_i is self-correlated. Lower rotational noise naturally corresponds to large values of τ_{r}, and we expect this time scale to approach infinity in the limit $D_{\mathrm{r}} \to 0$, as was discussed earlier in the context of the Vicsek model. Because we are mainly interested in the low effective-temperature regime, the τ_{r} time scale is unsuitable as our time characteristic. Instead, we consider the ballistic movement of the rod from equation 2.20, namely the self-propulsion speed v_{p}. We define the *ballistic time scale* [30]

$$\tau = \frac{\sigma}{v_{\mathrm{p}}} = \frac{\sigma \gamma_{\parallel}}{F_{\mathrm{p}}}. \tag{3.2}$$

This represents the length of time a rod uses to travel a length equal to its width σ at v_{p}. We can now characterize the interplay of translational and rotational motion by comparing the two time scales. We define a *persistence number* as

$$\mathrm{Pe}_{\mathrm{r}} = \frac{\tau_{\mathrm{r}}}{\tau} = \frac{F_{\mathrm{p}}}{\sigma \gamma_{\parallel} D_{\mathrm{r}}}. \tag{3.3}$$

This commonly goes by its alternative name, the (rotational) *Péclet number*, but "persistence number" may be less ambiguous as to its physical meaning. In units of rod width σ, this number defines the *persistence length* $S_{\mathrm{Pe}} = \mathrm{Pe}_{\mathrm{r}}\sigma$ over which an active rod has typically lost all information about its initial orientation [30]. Values of $\mathrm{Pe}_{\mathrm{r}} \gg 1$ represent the low-temperature domain, where the dynamics of the rod is dominated by translational movement. In the opposite case $\mathrm{Pe}_{\mathrm{r}} \ll 1$, we will expect more chaotic motion and a slower average drift velocity. Examples of random walks with different values of Pe_{r} are shown in Figure 3.1.

Usual values for Pe_{r} are largely dependent on the application of the model. Due to being associated with a characteristic distance of a particle's random walk, it is most relevant if directly compared to the size of a finite system. Low values generally correspond to negligible dynamical changes between weakly constrained and unconstrained systems, as these are unlikely to occupy a large area of influence. However, for magnitudes of Pe_{r} from $\mathcal{O}(10^2)$, rotational diffusion is strong enough to significantly affect the trajectories of interacting particles with characteristic size σ [35].
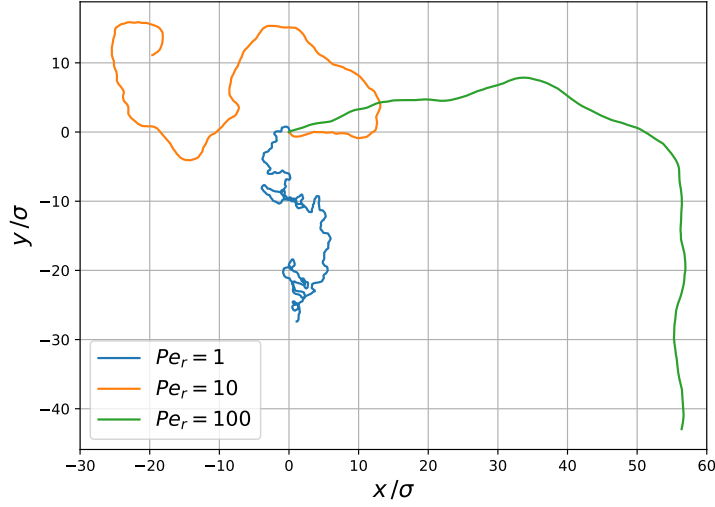
Figure 3.1: *Persistence and diffusion*: Positions of three independent ABRs ($A = 4$) tracked for a distance $S = 100\sigma$ ($\Delta t = 0.01\tau$), each with different values of Pe_r, showing the different random walk behavior. Increased noise shortens the persistence length, hence slowing the average drift from the initial position.

3.2.2 Strength of the repulsive interaction

While we defined the persistence number Pe_r, the set of equations describing the dynamics of our ABRs still contains three different energy scales: One each associated with the self-propulsion energy $F_p\sigma$, the rotational diffusion Pe_r and the height of the repulsive potential ϵ. Similar to how Pe_r relates the rotational diffusion to the strength of self-propulsion, we can define a single parameter to let us forget about the size of F_p entirely, and focus on the strength of the intermolecular forces acting between rods. Using the ballistic time scale τ defined by equation 3.2 as our time unit, we can express any time stamp as a dimensionless multiple of this unit, $t = \tilde{t}\tau$. Along with the reduced length $r = \tilde{r}\sigma$, we can reduce the translational ABR equations 2.20 and 2.21 to their dimensionless form:

$$\sigma \frac{\partial \tilde{r}_{i,\parallel}}{\partial(\tilde{t}\tau)} = \frac{1}{\gamma_\parallel} \sum_{j\neq i}^{N} F_{ij,\parallel} + \frac{1}{\gamma_\parallel} F_p$$

$$\Leftrightarrow \frac{\partial \tilde{r}_{i,\parallel}}{\partial \tilde{t}} = \frac{1}{v_p \gamma_\parallel} \sum_{j\neq i}^{N} F_{ij,\parallel} + 1$$

$$(3.4)$$

$$\sigma \frac{\partial \tilde{r}_{i,\perp}}{\partial(\tilde{t}\tau)} = \frac{1}{\gamma_\perp} \sum_{j\neq i}^{N} F_{ij,\perp}$$

$$\Leftrightarrow \frac{\partial \tilde{r}_{i,\perp}}{\partial \tilde{t}} = \frac{1}{2v_p \gamma_\parallel} \sum_{j\neq i}^{N} F_{ij,\perp}.$$

$$(3.5)$$

We obtain the dimensionless form of the repulsive force components $F_{ij,\parallel}$, $F_{ij,\perp}$ by inserting the dimensionless variables into the potential in equation 2.15

$$U_{\text{rep}}(\tilde{r}) = 4\epsilon \left[\left(\frac{1}{\tilde{r}}\right)^6 - \left(\frac{1}{\tilde{r}}\right)^3 \right] + \epsilon, \tag{3.6}$$

yielding the repulsive force

$$\begin{aligned}
\mathbf{F}_{\text{rep}}(\tilde{r}) &= -\frac{\partial}{\partial r} U_{\text{rep}}(\tilde{r}) \hat{\mathbf{r}} = -4\epsilon \frac{\partial}{\partial(\tilde{r}\sigma)} \left[\left(\frac{1}{\tilde{r}}\right)^6 - \left(\frac{1}{\tilde{r}}\right)^3 \right] \hat{\mathbf{r}} \\
&= \frac{\epsilon}{\sigma} \left[\frac{24}{\tilde{r}^7} - \frac{12}{\tilde{r}^4} \right] \hat{\mathbf{r}} = \frac{\epsilon}{\sigma} \tilde{\mathbf{F}}_{\text{rep}}.
\end{aligned} \tag{3.7}$$

When inserted back into equation 3.4, we obtain the fully reduced translational equation for the main axis direction

$$\frac{\partial}{\partial \tilde{t}} \tilde{r}_{i,\parallel} = \frac{\epsilon}{\sigma v_{\text{p}} \gamma_{\parallel}} \sum_{j \neq i}^{N} \tilde{F}_{ij,\parallel} + 1 = \beta \sum_{j \neq i}^{N} \tilde{F}_{ij,\parallel} + 1, \tag{3.8}$$

which contains only a single parameter $\beta \equiv \epsilon/\sigma v_{\text{p}} \gamma_{\parallel} = \epsilon/F_{\text{p}}\sigma$. By changing this parameter, we can control how the magnitude of the translational forces acting on the rods compare to each other. If we disregard changing the active driving force, we can interpret β as a comparative measure of the repulsion and translational friction $\gamma_{\parallel}$. $\beta \ll 1$ corresponds to softer collisions dominated by friction. For motion perpendicular to the rod axis, friction is doubled, and we get a similar equation from equation 3.5

$$\frac{\partial}{\partial \tilde{t}} \tilde{r}_{i,\perp} = \frac{\beta}{2} \sum_{j \neq i}^{N} \tilde{F}_{ij,\perp}. \tag{3.9}$$

3.2.3 Particle number

One of the most important subjects with regard to system realization is the particle number N used for each simulation. The main considerations here is to minimize the effects that a finite system size has on the results, all while being able to perform the calculations in a reasonable time. Regardless of anyone's definitions of reasonable, being able to make adjustments to the experiment and get useful results in hours rather than days contributes greatly to quality-of-life. Finding the balance between practicality and result quality is a universal challenge for computational work in scientific fields.

A computer implementation of the model will consider each particle to calculate interactions, making the total runtime scale by $\mathcal{O}(N^2)$[1]. Thus, a small particle number is preferred to avoid long runtimes. With the current state of computer

---

[1]This can be reduced to $\mathcal{O}(N)$ through the use of cell list algorithms, see Appendix A.

hardware speeds, particle numbers of magnitudes between $N = 10^2 - 10^4$ seem to have been the predominant choice in much of published research [23]. Larger numbers are required if we extend our implementation to 3D, typically by a factor $N^{3/2}$. Using a higher particle number in high-density systems is common due to the increased correlation length of particle variables. In earlier studies of ABRs at high densities, the steady state order parameters have been observed to be robust with respect to changes in N as long as N is of at least $\mathcal{O}(10^4)$ [27].

3.2.4 Effective area fraction

In the section concerning the Vicsek model, we used the number density ρ as the parameter of the system density. In that model, particles were treated as point-like particles of zero spatial extent. This is not the case for the ABP and ABR models, as repulsive interactions enforce separation between individual particles. As a more suitable density parameter, we will instead use the *effective area-* or *packing fraction*: The total fraction of the system area occupied by the particles. For circular particles, we use the effective diameter of the particles σ to define the effective area $\pi(\sigma/2)^2$. For a square system of dimensions $L \times L$ containing N particles, the packing fraction of the system is thus given by

$$\phi_{\text{circ}} = \frac{\pi}{4} \frac{N\sigma^2}{L^2}. \tag{3.10}$$

We intend to simulate systems of rods with $A > 1$, and thus the area of each particle needs to include the rectangular central segment. The generalized area fraction then becomes

$$\phi_{\text{rod}} = \frac{N\sigma\left(l + \frac{\pi}{4}\sigma\right)}{L^2} = \frac{N\sigma^2\left(A + \frac{\pi}{4} - 1\right)}{L^2}. \tag{3.11}$$

Naturally, $\phi_{\text{rod}} = \phi_{\text{circ}}$ for $A = 1$. It is important to point out that we consider soft particles with no well-defined dimensions. Depending on the potential we use, the effective area fraction may exceed $\phi > 1$, an effectively over-compressed system. As previously discussed, defining the effective rod width as σ is a somewhat arbitrary choice. However, as $U_{\text{rep}}(\sigma) = \epsilon$, we still conserve a form of generality.

3.3 Calculating repulsive forces

During a single collision, the forces between rods pairs will act reciprocally due to symmetry, $\mathbf{F}_{ij} = -\mathbf{F}_{ji}$. By recognizing this, half of the computational cost may be saved by only calculating the contact forces of specific pairs once. The question then becomes how to calculate the magnitude of $\mathbf{F}_{ij}$.

The task of calculating the repulsive forces between segmented particles such as in the rigid polymer model is rather intuitive in comparison, no doubt contributing to its popularity. For simplicity, we assume that the intermolecular forces between pairs of rods depend only on the shortest distance r_c between the two,

regardless of the total area of overlap [33]. The repulsive force then acts symmetrically in the centers-of-mass with a magnitude determined by this shortest distance. In a scenario where two rods are perfectly aligned, these points are not uniquely defined. With a floating-point machine epsilon of $\epsilon_\mathrm{m} \sim 10^{-16}$, we can neglect the possibility of this occurring. The problem is then simplified by one important observation: When computing the shortest distance points of two non-overlapping line segments, at least one of the contact points is an end-point of one of the line segments [36]. The second point is determined by computing the projection of the primary contact point onto the second line segment. Or, if the projected point is beyond the segment, take the nearest end-point and finally compute the distance between the obtained point pair.

The algorithm for finding the shortest distance between two rods i and j needs to be performed only once for a rod pair (i, j). For each pair, all four end-points and their corresponding contact points are calculated and compared, with the shortest being selected to determine the force vector $\mathbf{F}_{ij}$. A schematic of the interaction forces is shown in Figure 3.2.
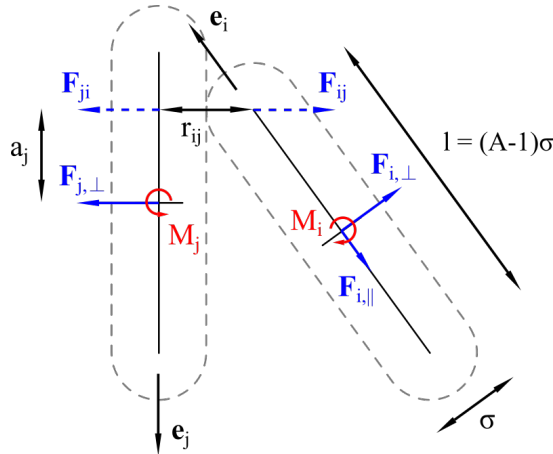
Figure 3.2: *Rod interaction*: Schematic of the interaction of a pairwise rod collision, showing the center-of-mass translational forces and accompanying rotation.

3.4 Integrating the equations of motion

Because we simulate our active systems with computers, we require a method of approximating the solutions to the equations of motion from Sections 2.4 and 2.5. Unlike purely deterministic differential equations, our set of equations are partly stochastic; they contain a random element in the form of the rotational diffusion term $\sqrt{2\tilde{D}_\mathrm{r}}\xi$. Finding the solution to these equations is therefore reminiscent of Monte Carlo simulations, in that we observe statistical averages (e.g. diffusion) emerge from individual realizations from some probability distribution. From the longitudinal and transverse velocity components given by the first-order equa-

tions 2.20 and 2.21, we obtain the new positions of every rod by calculating their change at a finite number of points in time. This method requires discretization of time $\Delta t = \Delta\tilde{t}\tau$ to calculate new trajectories and positions. A simple approximation of the solution can be found by using the first-order Euler-Maruyama scheme

$$
\begin{aligned}
\tilde{r}_{i,x}(\tilde{t}+\Delta\tilde{t}) &= \tilde{r}_{i,x}(\tilde{t}) + \Delta\tilde{t}\cos\theta_i\,\beta\Big(\sum_{j\neq i}^{N}\tilde{F}_{ij,\parallel}+1\Big) - \Delta\tilde{t}\sin\theta_i\,\frac{\beta}{2}\sum_{j\neq i}^{N}\tilde{F}_{ij,\perp} \\
\tilde{r}_{i,y}(\tilde{t}+\Delta\tilde{t}) &= \tilde{r}_{i,y}(\tilde{t}) + \Delta\tilde{t}\sin\theta_i\,\beta\Big(\sum_{j\neq i}^{N}\tilde{F}_{ij,\parallel}+1\Big) + \Delta\tilde{t}\cos\theta_i\,\frac{\beta}{2}\sum_{j\neq i}^{N}\tilde{F}_{ij,\perp},
\end{aligned}
\tag{3.12}
$$

for $\tilde{t}_0 \leq \tilde{t} \leq \tilde{t}_{\max}$. These equations of course assume that every particle has an identical internal self-propulsion force generating a swim speed $v_p = \sigma/\tau$ along $\mathbf{e}_i$, but this term is thrown out for passive particles. From the dimensionless form of the rotational equation of motion 2.11

$$
\frac{\partial}{\partial\tilde{t}}\theta_i = \frac{\epsilon\tau}{\gamma_r}\sum_{j\neq i}^{N}\tilde{M}_{ij} + \sqrt{2\tilde{D}_r}\xi(\tilde{t}),
\tag{3.13}
$$

with $\tilde{D}_r = D_r\tau$. We similarly integrate the stochastic differential equation for $\partial_{\tilde{t}}\theta_i$, using the time step $\sqrt{\Delta\tilde{t}}$, as the rotational diffusion makes each position coordinate change proportionally to $\sqrt{\tilde{t}}$ [34]

$$
\theta_i(\tilde{t}+\Delta\tilde{t}) = \theta_i(\tilde{t}) + \Delta\tilde{t}\,\frac{6\beta}{A^2}\sum_{j\neq i}^{N}\tilde{M}_{ij} + \sqrt{2\tilde{D}_r\Delta\tilde{t}}\xi(\tilde{t}).
\tag{3.14}
$$

$$
\langle\xi_i(\tilde{t})\rangle = 0, \quad \langle\xi_i(\tilde{t})\xi_j(\tilde{t}')\rangle = \delta_{ij}\delta(\tilde{t}-\tilde{t}')
$$

Due to being a first-order method, the Euler-Maruyama scheme has an error of $\mathcal{O}(\Delta\tilde{t}^2)$ [34], meaning that it is accurate to $\mathcal{O}(\Delta\tilde{t})$. It approximates the solution in an unsymmetric way, as only the derivative at the beginning of the time interval $\Delta\tilde{t}$ is considered for the trajectory calculation. Another problem with this first-order scheme is that accuracy is only improved by using a smaller time step $\Delta\tilde{t}$. Complete convergence of the solution is after all asymptotic, which only holds for $\Delta\tilde{t} \to 0$. Decreasing the time step does however proportionally increase computational runtime. Accuracy may be improved otherwise by using multistep-methods such as the Runge-Kutta methods, which uses information at several time stamps for the approximation. By doing this, these methods may gain accuracy in the range of $\mathcal{O}(\Delta\tilde{t}^3)$ to $\mathcal{O}(\Delta\tilde{t}^5)$. However, the stochastic element of the equations pose an issue for higher-order methods, especially when noise is dominant. Because we have to rely on this not being the case, the Euler-Maruyama scheme is usually sufficient, and thus one of the most commonly used methods. Improved methods such as the Adams-Bashforth method improve stability by using an implicit scheme, although it is still first-order accurate for the stochastic noise.

Chapter 4

Investigating steady state of dense ABR systems

4.1 Non-equilibrium jamming transition

As mentioned in the introductory chapters, much of the interest surrounding active matter systems is related to the non-equilibrium phase transitions associated with them. Specifically with regard to dense systems, their comparison to the *glass transition* observed for passive systems. This transition is observed when freely flowing thermal particles experience a dramatic slowdown at critical densities and temperature [2]. Although active systems are not at thermodynamic equilibrium due to self-propulsion, ABP systems possess a non-equilibrium steady state for densities lower than the critical density for the glass transition [2]. Below this density, we find a partially liquid-like flowing system sustained by the self-propulsion of the active particles.

As particles come into contact and create regions of high density, the motion of individual particles within these regions is inhibited. As this *dynamical arrest* becomes system-wide, we observe a phase transition into a *jammed* solid-like state. The equilibrium equivalent phase transition is the *glass transition*, where high densities and low noise gives the bulk material solid-like properties when subject to external forces [6]. Unlike in the passive case, the active jamming phenomenon is not fully understood in terms of the few parameters of temperature and density, and the nature of the transition has been related to both non-equilibrium particle interactions and boundary conditions.

We conduct an investigation to characterize the flow-jamming transitions of active particles with the model and parameters outlined in previous chapters, with most attention given to the rod aspect ratio A and the effective area fraction ϕ. The initial task will be to make general observations from the model, and make comparison with earlier findings of similar setups.

4.1.1 Effective diffusion of ABRs

In the first practical implementation of the ABR model outlined in Chapter 2, we examine the properties of a system of short rods in periodic boundary conditions, similarly to the treatment of the Vicsek model. With the now extensive rods, the nature of the interparticle interactions are completely different. Collisions between rods will cause rods to speed up, slow down or rotate, generating behavior which may differ noticeably depending on certain system parameters. The frequency of these collisions is determined primarily by the effective area fraction ϕ, and so we want to understand how the density impacts the dynamics of an ABR system.

In order to quantitatively describe the dynamics of a system, we can use the *mean squared displacement* (MSD), defined by the ensemble average [30]

$$\text{MSD} \equiv \langle |\mathbf{r}(t) - \mathbf{r}_0|^2 \rangle = \frac{1}{N} \sum_{i=1}^{N} |\mathbf{r}^{(i)}(t) - \mathbf{r}_0^{(i)}|^2, \tag{4.1}$$

where $\mathbf{r}_0$ is the reference position of particle i at $t = 0$. By tracking the particle ensemble in time, we can make some general remarks about its collective motion from this reference state. The MSD defines an effective diffusion coefficient D_{eff} for the ensemble [30]. Expanding equation 4.1 for 2D movement of a single independent ABR obeying equations 2.20 and 2.11 we get the expression for $\langle |\mathbf{r}(t) - \mathbf{r}_0|^2 \rangle = \langle \Delta r^2(t) \rangle$

$$\langle \Delta r^2(t) \rangle = v_{\text{p}}^2 \tau_{\text{r}} t - \frac{v_{\text{p}}^2 \tau_{\text{r}}^2}{2} \left(1 - e^{-2t/\tau_{\text{r}}} \right), \tag{4.2}$$

which we for convenience and clarity can rewrite to the dimensionless form

$$\sigma^2 \langle \Delta \tilde{r}^2(\tilde{t}) \rangle = v_{\text{p}}^2 \text{Pe}_{\text{r}} \tau^2 \tilde{t} - \frac{v_{\text{p}}^2 \text{Pe}_{\text{r}}^2 \tau^2}{2} \left(1 - e^{-2\tilde{t}/\text{Pe}_{\text{r}}} \right)$$

$$\Leftrightarrow \langle \Delta \tilde{r}^2(\tilde{t}) \rangle = \text{Pe}_{\text{r}} \tilde{t} - \frac{\text{Pe}_{\text{r}}^2}{2} \left(1 - e^{-2\tilde{t}/\text{Pe}_{\text{r}}} \right). \tag{4.3}$$

For times small compared to the persistence time, $\tilde{t} \ll \text{Pe}_{\text{r}}$, this expression reduces to $\langle \Delta \tilde{r}^2(\tilde{t}) \rangle = \tilde{t}^2$. Because the self-propulsion of the rod is linear in time, the trajectory is ballistic (MSD $\sim \tilde{t}^2$) at these small times. In the long time limit $\tilde{t} \gg \text{Pe}_{\text{r}}$, the MSD is approximated by $\langle \Delta \tilde{r}^2(\tilde{t}) \rangle = \text{Pe}_{\text{r}} \tilde{t}$. Rotational diffusion leads to randomization in the direction of the self-propulsion, and the result is a diffusive trajectory (MSD $\sim \tilde{t}$). From measuring the mean squared displacement, we can define an effective diffusion coefficient $\tilde{D}_{\text{eff}}$ for the system by

$$\langle \Delta \tilde{r}^2(\tilde{t}) \rangle = 4 \tilde{D}_{\text{eff}} \tilde{t}.$$

$$\Leftrightarrow \tilde{D}_{\text{eff}} = \frac{\langle \Delta \tilde{r}^2(\tilde{t}) \rangle}{4\tilde{t}} \tag{4.4}$$

In transient systems, the effective diffusion constant D_{eff} cannot be assumed constant, because the time dependency of the correlation functions.

4.2   Summary of system parameters

Table 4.1

Quantity	Symbol	Dimensions	Dim.less form	Value
Rod number	N	1	N	1200-2400
Rod width	σ	L	1	Length unit
Rod aspect ratio	A	1	A	$2, 4, 6$ or 10
Potential energy	ϵ	GL^3	$\beta = \frac{\epsilon}{F_p\sigma}$	0.1
Friction coefficient	γ_0	GT	1	Modulus unit
Self-propulsion force	F_p	GL^2	1	Time unit
Rot. diff. coefficient	D_r	T^{-1}	$\mathrm{Pe_r} = \frac{F_p}{A\sigma^2\gamma_0 D_r}$	To be varied
Effective area fraction	ϕ	1	ϕ	To be varied

Table 4.1 summarizes the parameters derived in Section 3.2. For the simulations we therefore operate with the parameter space $\{A, \beta, \mathrm{Pe_r}, \phi\}$. Because we control for area fraction ϕ instead of N, this number fluctuates in the range $N \in [1200, 2400]$. Instead of having a dedicated alignment strength parameter, which is necessary in models of isotropic particles emulating alignment [37], the rod aspect ratio A acts as an effective alignment strength parameter for our model [38]. The self-propulsion force F_p, our unit of force, both defines the time unit though the active velocity v_p and the energy scale $F_p\sigma$. Using the value $\beta = 0.1$ for the dimensionless repulsion strength parameter was selected after running tests of the system and was shown to provide better stability for longer rods, due to reducing the magnitude of the alignment torque. Since the high-density characteristics of the system has an unknown dependency on the repulsion strength, we prioritize staying consistent even though this value could safely be larger for short rods.

4.2.1   Rod aspect ratio

For the spherocylindrical model we chose to represent the ABRs in Chapter 2 to be of any use, we should make an informed decision of which values of the rod aspect ratio A we consider in our simulations. We ideally want to cover a wide range of values to adequately explore the phase behavior. It is known that the phase behavior of elongated particles is qualitatively different from spherical ones, even when the asphericity $\Delta A = \mathcal{O}(10^{-6})$ [39]. In this range, special theory will be needed for adequate description. As a more general low-aspect case, we choose $A = 2$ to be the minimum asphericity.

   Intermediate ratio values, $A \sim 5$ have been used in models of dense layers of bacteria [4]. Separating this range into $A = 4$ and $A = 6$ will allow us to more easily spot differences within characteristically similar steady states, as well as

offering better data continuity. The value $A = 6$ has also been used in studies of nematically ordering vibrated copper wire segments [40].

We will make an additional investigation of rods with aspect ratio $A = 10$. Although this represents a rather extreme case of particle anisotropy, it is not one overlooked in active matter literature. Earlier studies have investigated arrangements of human melanocytes [41], pigment skin cells about 100μm in length. However, these are naturally flexible, meaning that a rigid rod model may be overly reductionist in this biological context. Lengths exceeding $A > 10$ are typically used in simulations of elastic flagella [38] where hydrodynamic interactions play an important role. These cases are therefore beyond the scope of this thesis.

4.3   ABRs in periodic domain

Large systems of rods with aspect ratio $A = 4$ were run for different values of ϕ, and the MSD was measured for a $\tilde{t} = 100$ time interval ($\Delta \tilde{t} = 10^{-3}$) after an equally long initialization phase[1]. Given the effective size of the system, these relaxation times are required for the system to enter a steady state and avoid measurements in the transient period. The persistence number is fixed to $\text{Pe}_{\text{r}} = 10^3$, corresponding to an extremely low noise regime. As observed in simulations of the Vicsek model, low noise promotes a higher degree of clustering and ordering. This value will ensure that we can attribute the observed behavior mainly to the overdamped interactions between rods. The measured MSD is shown in Figure 4.1(a) and state snapshots of some of the systems are shown in Figure 4.2.

4.3.1   Ordering and flocking

After starting from a highly ordered initial state, the rods quickly form small clusters as they begin to collide with each other. Unlike the unlimited density of clusters we can observe in the Vicsek model, the repulsive forces between rods create a competition of attraction and repulsion [42]. Because of the long persistence length $\text{Pe}_{\text{r}}\sigma = 10^3\sigma$ in comparison to the system size $L \sim 10^2\sigma$, the breakup rate for these clusters is long, meaning that they too persist for long periods of time. This in turn lets clusters live long enough to collide and merge with other clusters. The clustering and flocking behavior is an example of *motility-induced phase separation*, a separation phenomenon observed universally in self-propelled repulsive particles, even in systems without extrinsic alignment [14].

Visual inspection of Figures 4.2 and 4.3 shows that the ordering scheme of the elongated rods seems to be one characterized by a *smectic* phase, a mesomorphic phase characterized by a 1D translational correlation between ordered rods [1]. This manifests as long bands of packed rods with widths commonly exceeding multiple rod lengths $A\sigma$. The bands may then combine in a zipper-like manner with other similarly oriented bands and create regions of highly ordered grid-like

---

[1]See appendix A for a detailed description of the system initialization.

configurations. This is a result of the special geometry of the spherocylindical rods, as rods tend to align more strictly to their neighbors as opposed to ellipsoidal rods. Rods with reverse orientation may become trapped within bands if restricted by the local density. The average width of bands with continuous polarity thus seems to increase from lower to moderate density, as the increased collision frequency leads to higher local orientational correlation. From moderate to high densities, the width decreases from an increased number of trapped "imperfections", as well as larger jammed regions suppressing the formation of wider bands.

4.3.2 Active jamming transition

For these chosen parameter values, we are located in the $\tilde{t} \ll \mathrm{Pe_r}$ regime for independent rods, meaning that would expect the MSD of freely moving rods to grow exponentially with $\sim \tilde{t}^2$. With periodic boundary conditions, this is observed for $\tilde{t} < 40$, followed by a more linear evolution. This corresponds to a slowing of the dynamics caused by dense rod clustering. Higher densities directly result in lower measured MSD. Equation 4.2 yields a theoretical value of $\mathrm{MSD}(\tilde{t} = 100) \approx 9.4 \cdot 10^3 \sigma^2$, or an effective translational diffusion constant $\tilde{D}_{\mathrm{eff}} = 23.5$, which acts as the upper bound value of these measurements. The ballistic $\tilde{t}^2$-regime is also shortened from the translational dynamic arrest, and we observe a diffusive $\sim \tilde{t}$ behavior when the ratio of the ballistic and rotational time scales changes. It is shown that for systems of passive particles, jamming is associated with a specific critical density ϕ_c, while for active systems, flocking leads to the formation of dense clusters with a local density ϕ_c. It has also been shown that this critical density increased with increased activity in the system [6].

**(a)** $A = 4$. **(b)** $A = 4$ in a square channel.
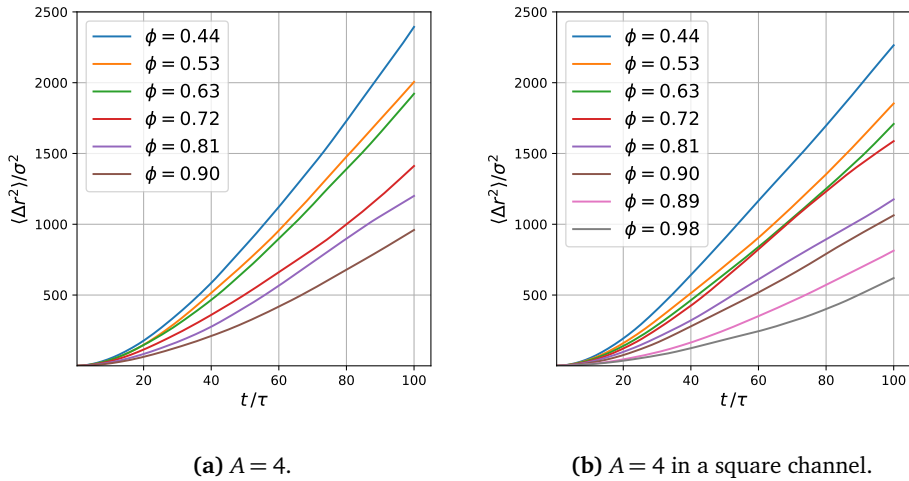
Figure 4.1: *Density and diffusion*: Mean-squared displacement calculated for a of systems of different packing fractions ϕ, showing the emergent $\Delta \tilde{r}^2 \sim \tilde{t}^{\frac{3}{2}}$ superdiffusive behavior of the active rods. Rods confined to a channel experience an earlier onset of movement on a diffusive time scale for similar densities.

As mentioned in the introductory chapter, one important area of ongoing research on this type of phase behavior is in the biophysical field concerning systems of cells. The jamming of cell layers is a field of research separated from the chemical aspects of cells. It is instead focused on how the mechanics of individual cells and larger cell ensembles forms larger structures through symmetry-breaking interactions. The movement of cells is important to maintain the tissue in the body, both in formation of new tissue and in repairing damage [11]. Collections of cells have for a long time been treated as viscoelastic liquids which exhibit behavior as solid-like on short time scales and as viscous liquids at long time scales [43]. Dense clusters of cells move collectively at large time scales, but as each cell is constrained in their movement from the crowded environment, the clusters are solid-like at short time scales. This amorphous solidification is attributed largely to density, but also the cell-cell interactions caused by their shape, as well as adhesion [44]. The rigid rods emulate this behavior in many ways. However, living cells change their shape and respond to their environment dynamically, and making a good comparison of theses systems is therefore difficult.

Understanding jamming and un-jamming of cellular tissue also has applications in the field of cancer research. Metastasis, the process by which cancerous cells split off from an aggregate, migrate and spread to other locations in the body, works much like the healthy processes of tissue maintenance [43].

(a) $\phi = 0.44$

(b) $\phi = 0.63$

(c) $\phi = 0.81$

(d) $\phi = 0.90$
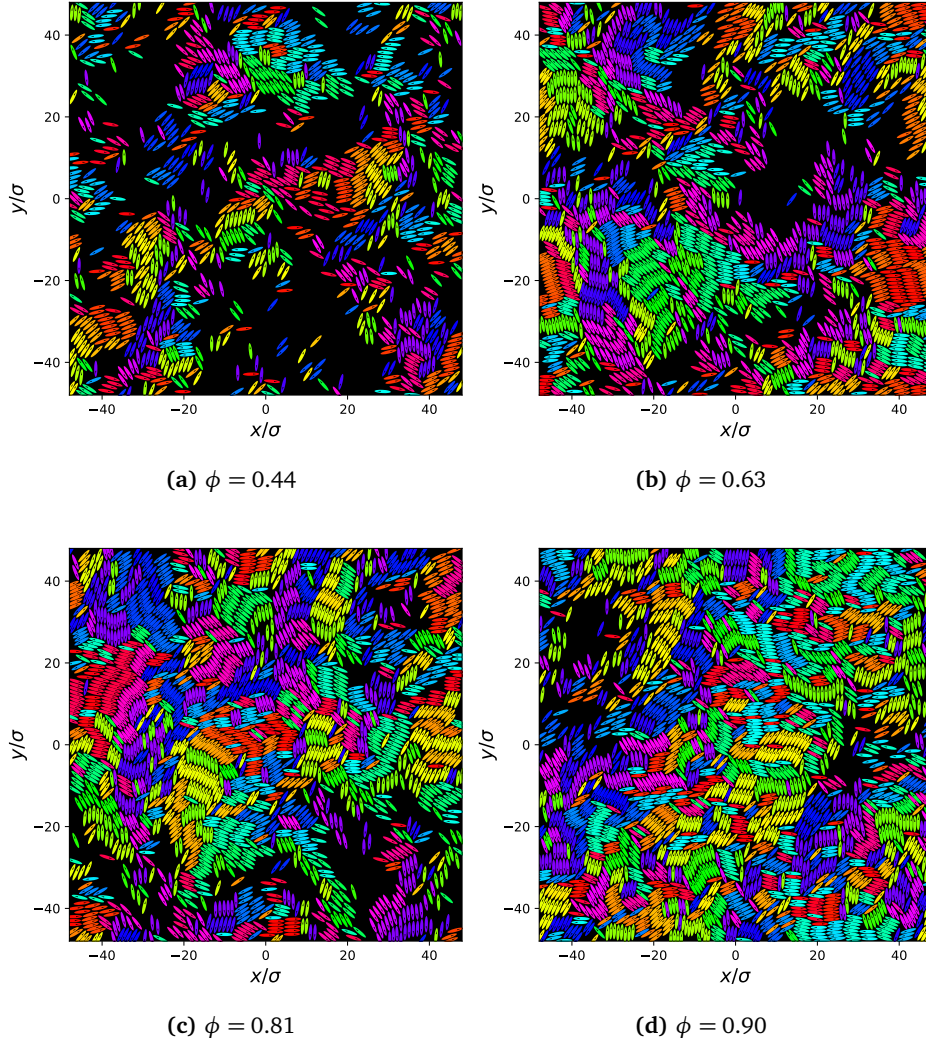
Figure 4.2: *Unbounded rods*: **(a-d)**: Snapshots of some $A = 4$ systems with periodic boundary conditions after running for a total time $t = 200\tau$. Controlling for density, particle numbers range $N \in [1300, 2400]$. $\mathrm{Pe_r} = 10^3$, $\beta = 0.1$. Rod colors correspond to 2D orientation. The ellipsoid used to draw the rods does not correspond to the shape or cut-off of the repulsive potential, but is rather for illustrative purposes.

4.4   Bounded domains: Channel

The idealized infinite system emulated by periodic boundaries demonstrate the emergence of clusters in systems of active colloids. Studying the behavioral properties of active agents in more complex environments, however, reiterates their utility in understanding real biological processes. Focusing on the relatively simple mechanics of microscopic swimmers, these life-forms rarely swim alone or in unbounded fluids [35]. Interaction between individual active particles comes with some set of effects, while barriers and obstacles represent other system influences entirely. The main function of obstacles is restricting the size of the system, and thereby limiting the infinite-system effects we cannot avoid with fully periodic boundary conditions.

We would like to make a focused effort to investigate the effects on an active system confined to a channel, an environment allowing for unbounded movement along only a single axis. Previous work has shown a prominent feature of this constraint, namely an aggregation of particles close to the barrier which defines the channel. This arises with a corresponding depletion layer near the channel center line [45]. As one might predict, this is due to the time it takes for rotationally diffusive particles to reorient away from the barrier, an asymmetry causing particles to tend to spend time at the obstacle. This phenomenon persists even in systems where particles only interact with the wall itself [46][14]. Systems of repulsive spherical particles allow for a similar treatment, and have even been shown to exhibit stronger accumulation at a wall than elongated rods [35]. These studies frequently consider the ratio of the persistence length to the wall separation distance, i.e. the channel width. As we have put a large focus on the quite flexible model of continuous active rods, we naturally want to find similar relationships between the rod shape and the collective behavior of our system.

As far as we know, systems of elongated active rods in this type of boundary conditions have not been studied extensively. Work by Wensink and Löwen have made connection between microscopic interactions and the transient behavior [47] and characterized phases for periodic boundary conditions [27]. Our contribution will be exploratory in terms of summarizing these observations and conduct an investigation of the hybrid rod model. This makes the methodology an important topic of later discussion along with the results themselves.

4.4.1   Method

The channel was implemented by arranging a line of stationary rods separated by a distance $l = (A-1)\sigma$ on one side of the domain. The barrier is thus exclusively repulsive, and does not impose a no-slip condition on the system. As the rods are fixed in position, they are not impacted by the overlapping occurring on each rod end, and the separation distance l ensures that the barrier has a relatively smooth

profile[2]. Due to the already enforced periodic boundary conditions, the single line of rods restrict all movement beyond $-L_x/2 < x < L_x/2$, but rods are free to move infinitely in the $\pm\hat{y}$-directions.

We first made a general assessment of the behavior of active systems confined to a 2D channel, and later make more focused considerations of the relation between the length of rods, the effective area fraction and the properties of the channel itself. Several $A = 4$ systems were simulated with different packing fractions for a time $t = 200\tau$ after being allowed to run for 100τ from an ordered initial state. The measured MSD for the different densities is shown alongside the results for periodic boundary conditions in Figure 4.1, and snapshots in Figure 4.3. The persistence number was again fixed as $\mathrm{Pe_r} = 10^3$ to have a weak influence, given a channel size $L \ll \mathrm{Pe_r}$.

4.4.2 Flow order parameters

From the measured MSD and visual inspection of Figure 4.3, we start to notice dissimilarities to the systems with periodic boundary conditions. The introduction of a barrier leads to a slight slow-down of the dynamics, due to rods stagnating at the wall. This edge effect is reflected in the fact that rods aggregate massively along the wall, even for low effective area fractions of $\phi = 0.29$ and $\phi = 0.39$. Aggregation of active systems in confinement is nothing new, and has been shown to occur in both channels and in circular confinements [49]. The dense regions we observe along the wall are ordered largely in a similar manner to Figure 4.2, although some rods become entrapped within the formed boundary layer, causing imperfect smectic-nematic ordering. From visual inspection, it is unclear whether the frequency of these band-disrupting regions increases with density, because of the conflict between individual entrapment and higher density of rods overall. The various similarities and dissimilarities between the types of boundary conditions motivate an adjusted experiment to further investigate effect observed close to the barrier.

To quantify the dynamical behavior in the channel, we propose a similar treatment to the mean squared displacement for systems subject to periodic boundary conditions. We use the average $\hat{y}$-component of the velocity in some region to define the flow parameter

$$\bar{v}_y = \frac{1}{n}\left| \sum_{j=1}^{n} \mathbf{v}_j \cdot \hat{\mathbf{y}} \right|, \tag{4.5}$$

along the channel, where n is the number of rods j within a sub-domain of

---

[2]Because the rods are not rectangular, the areas where the "rod caps" overlap create regions of overlapping potentials, and thus the barrier is not perfectly uniform. While avoiding overlap, separating the rods by $A\sigma$ would create areas where the repulsive potential height is finite, possibly causing rods to penetrate the barrier in extreme cases. Uneven or rugged boundaries, such as the one used in [48] may be deliberately incorporated to suppress global translation modes, in this case vortex formation along a circular boundary.

(a) $\phi = 0.29$

(b) $\phi = 0.39$

(c) $\phi = 0.49$

(d) $\phi = 0.58$

(e) $\phi = 0.69$

(f) $\phi = 0.78$

(g) $\phi = 0.89$

(h) $\phi = 0.98$
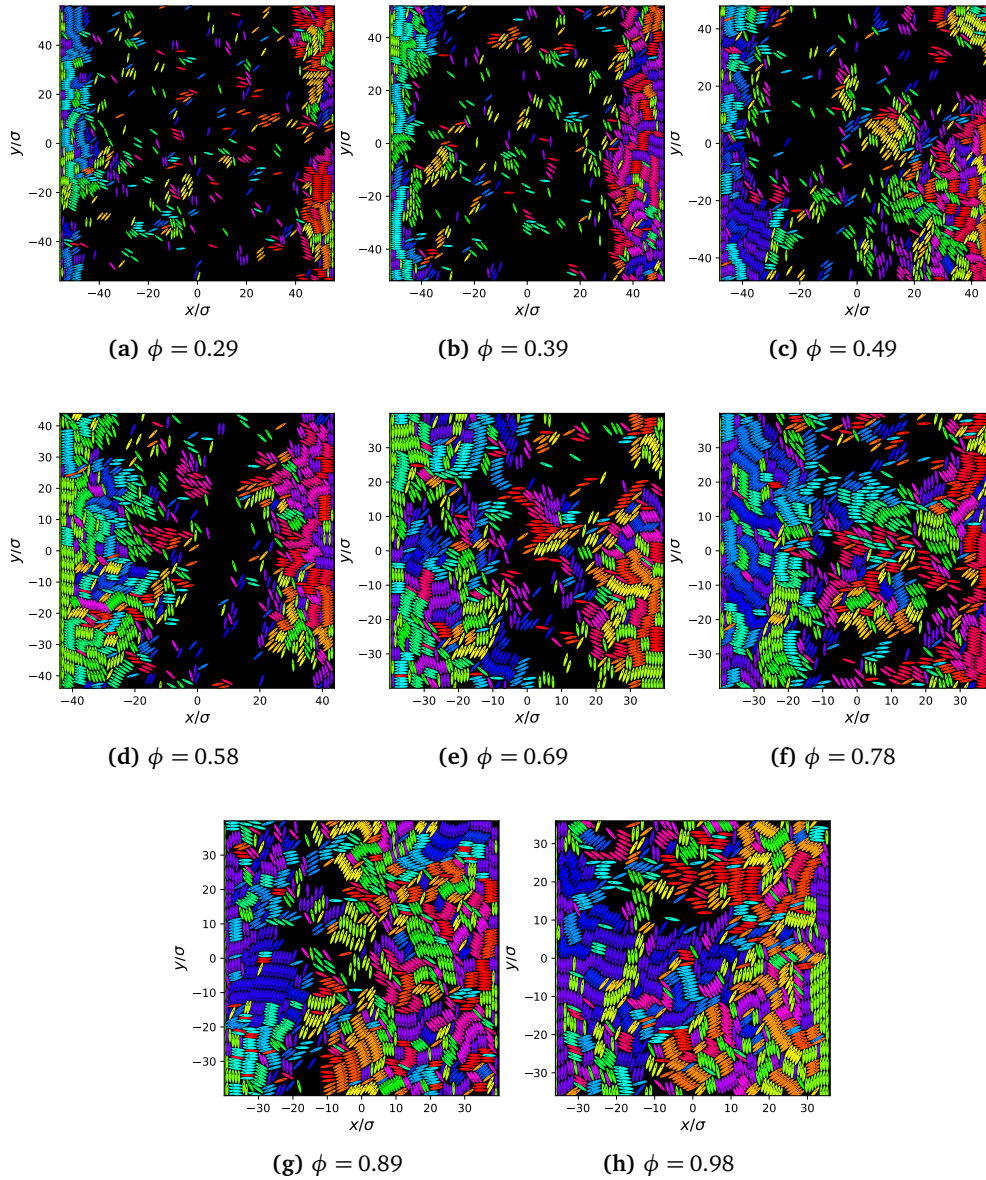
Figure 4.3: *Channel*: **(a-h)**: Snapshots for $A = 4$ systems in a square $\hat{y}$-directed channel after a total runtime $t = 300\tau$. Controlling for density, particle numbers range $N \in [1000, 1600]$. $\mathrm{Pe_r} = 10^3$, $\beta = 0.1$. Colors correspond to 2D orientation.

dimensions $(\Delta L_x, L_y)$. Similarly, we define the absolute flow parameter

$$\bar{u}_y = \frac{1}{n} \sum_{j=1}^{n} \left| \mathbf{v}_j \cdot \hat{\mathbf{y}} \right| \tag{4.6}$$

to quantify overall $\hat{y}$-directed motion. With $\bar{v}_y$, we aim to observe net movement along sections of the channel, and describe any flow patters that may emerge. $\bar{u}_y$, on the other hand, makes it easier to point out areas of stagnation, regardless of the direction. Large fluctuations in the flow parameters can indicate the onset of new phases, and allow us to make a quantitative description of these phases. The coarse-graining domain width was chosen to be $\Delta L_x = \sigma$.

Due to the moderate-to-high density regime we will investigate, periodic boundary conditions inevitably produce some self-correlations in the rods' positions. As we want to investigate the effects of the imposed barrier specifically, the channel has been expanded to dimensions $L_x \times L_y$, where $L_y = 2L_x$ to suppress the influence of the periodic channel. We choose an effective temperature $\mathrm{Pe_r} = 10^2$, a value that exceeds the width L_x for most systems and thus allows the barrier to be the dominant influence on the dynamics. It is also biologically justified by the fact that real cell motion is usually highly persistent. This is due to it being more efficient in searching for chemotactic signals than a pure random walk [50].

We ran systems for a range of rod aspect ratios $A \in 2, 4, 6, 10$ with packing fractions $\phi = 0.6$. Additional runs with higher packing fractions $\phi = 0.9$ were performed for $A = 2, 10$ to probe the density-dependency of the extreme cases. Each permutation was realized three times for later averaging, and was run for $t = 300\tau$, where the transient phase was included to gain understanding of the transition to a steady state. The simulations were carried out with a time step $\Delta t \in [5 \cdot 10^{-4}, 5 \cdot 10^{-3}]\tau$. Flow profiles of the subregions troughout the time interval are shown in Figure 4.4, and snapshots of the final states are shown in Figure 4.5. Results from the high-density systems are shown in Figure 4.6.

4.4.3 Short rods: Boundary layer formation

A priori, we expect an aggregation of rods along the barrier. The lowest effective area fraction $\phi = 0.6$, although rightfully regarded as a very high density, allows for relatively free movement of rods. Thus, the diffusive behavior from an initial state will be somewhat similar to the open boundary scenario. A curious observation from the $A = 2$ systems is the formation of a highly ordered boundary layer oriented perpendicular to the barrier. The steady state is otherwise characterized by a dilute liquid domain in the interior of the channel. This position distribution is known to be a feature of self-propelled rods in confinement, and the surface excess is shown to increase with activity [51]. Some of these studies consider hydrodynamic interactions with the barrier, which promotes alignment parallel to the wall. We see the formation of bands which spontaneously push perpendicularly towards the wall, something not observed in these studies. This is especially interesting given that the initial condition is completely nematically ordered along

the $\hat{y}$-direction. The absolute system flows in Figure 4.8(a) reflect the observed steady state, with a sharply decreasing flow in the early transient period, followed by consistent movement determined by the density-dependent central region.

4.4.4   Intermediate rods: Active turbulence

The most apparent observation for rods in the intermediate and long A-range $A > 2$, is that we see overall more ordered configurations emerge. Net flow measurements in Figure 4.4 indicate that in the early transient phase, these systems form small collectively moving clusters. The direction of this movement is alternating between $\pm\hat{y}$. For $A = 4$ and $A = 6$, this flow regime slowly disintegrates. Because the flow is highly correlated with the initial state, rotational diffusion will break up the areas of high nematic order and towards a steady state which is more characteristically turbulent. We see a sharp decline in absolute flow during this process, with the decline being significantly slower for $A = 6$.

Along the boundary, we no longer observe the same type of ordered boundary layer formation. The aggregated layer is instead composed of several locally ordered bands, interrupted by highly disordered regions. Most notably, the innermost layer is now in equal parts aligned with the barrier, and this fraction seems to increase with longer rod lengths. Moving towards the center, this wall-aligned layer is followed by an irregular layer of perpendicular rods. This layer is partly "nematized" for $A = 6$ at $t = 300\tau$, indicating that longer rods are more likely to align with the wall at long times. The onset of higher nematic order is reflected in both Figures 4.7(c,d) and 4.8. After a transient dynamical arrest, the system experiences an emerging shear flow along the barrier. The central region seems to remain disordered and turbulent, as parallel movement along the wall is more likely to reflect rods back to the center. Active turbulence has been studied in the context of bacterial motion, where nematic ordering causes high-vorticity dynamics in dense systems [52].

4.4.5   Long rods: Lane formation

For long rods, $A = 10$, we observe the emergence of separated flowing lanes that remain intact for long periods of time. For low densities, the lanes merge and allow for $\hat{y}$-directed regions of highly correlated flow fields. In the long time limit, we can hypothesize that the system will reach a state with three separated lanes of alternating direction. An alternative would be one with two lanes, although this may be less likely due to the difficulty for the central lane to completely dislocate one of the boundary lanes. This type of left-right symmetry breaking shear flow is observed in confined systems of hydrodynamically moving cells at critical channel widths, due to mechanical instability [18]. At higher density, our measured flows indicate that the system forms narrower lanes or lanes that more frequently overlap, causing a near-zero net flow in these regions and decreased overall flow (Figure 4.8(d)). It has been shown that this laning phase can be achieved in systems with periodic boundary conditions when above a certain rod length and density

(a) $A = 2$

(b) $A = 4$

(c) $A = 6$

(d) $A = 10$
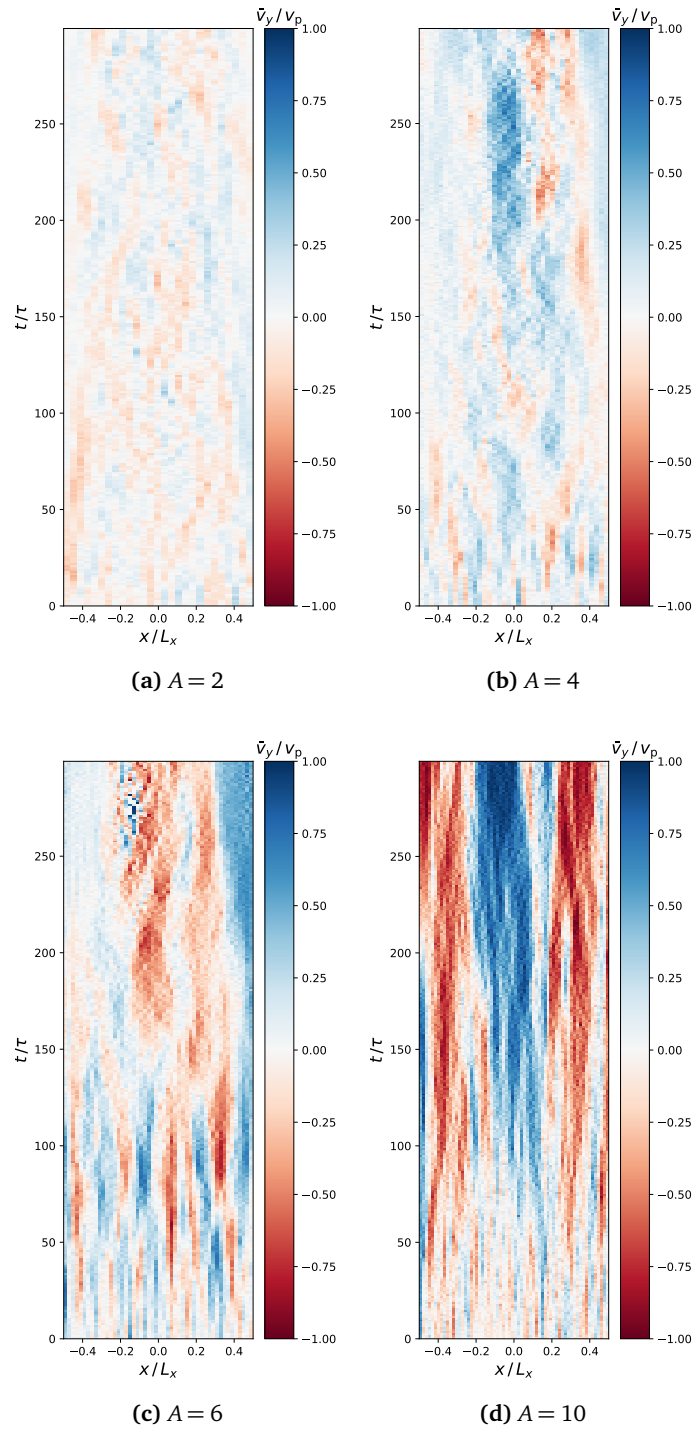
Figure 4.4: *Flow in channel*: **(a-d)**: Example heatmaps of the net flow profile in time for individual simulations from the initial state to $t = 300\tau$. $\phi = 0.6$, $\beta = 0.1$, $\mathrm{Pe_r} = 10^2$, $N = 2048$.

(a) $A = 2$

(b) $A = 4$

(c) $A = 6$

(d) $A = 10$
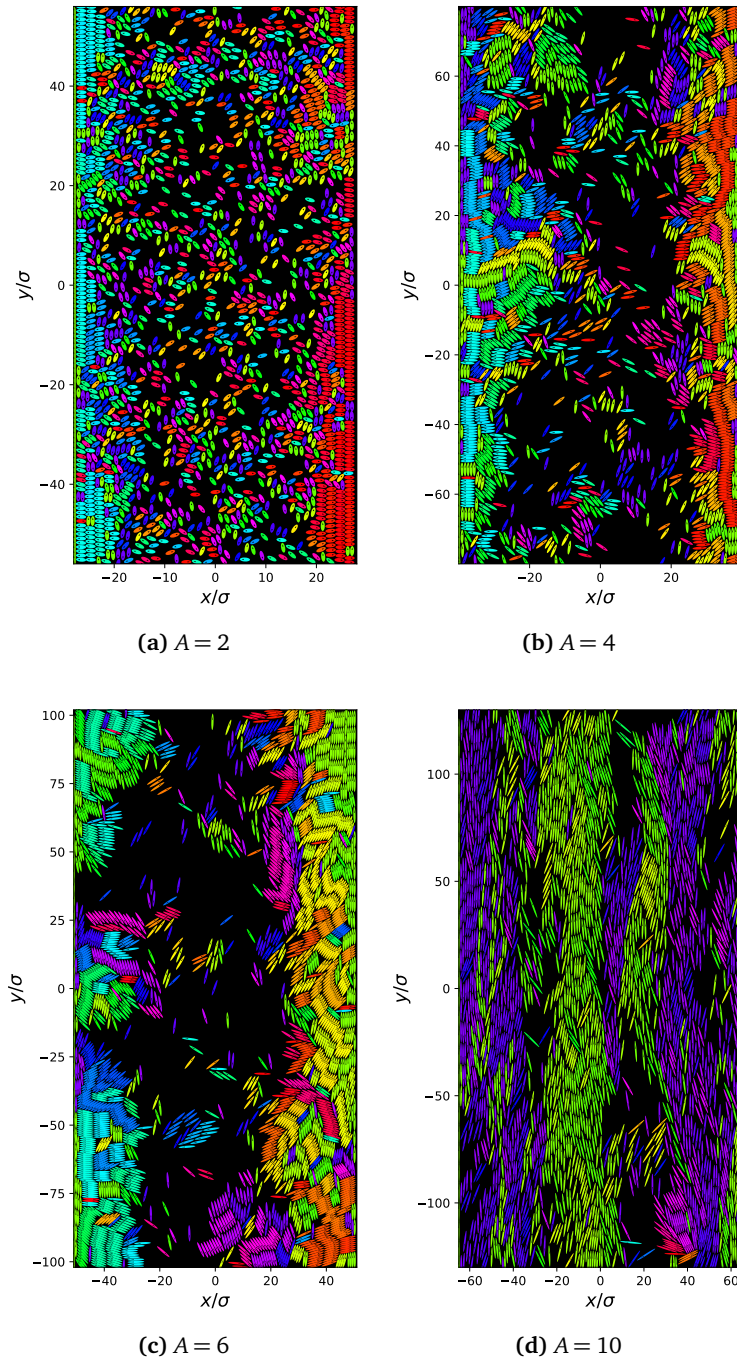
Figure 4.5: *Changing dynamics*: **(a-d)**: Snapshots of the $t = 300\tau$ states of the systems corresponding to Figure 4.4, showing the features observed for different values of the rod aspect ratio A. $\phi = 0.6$, $\beta = 0.1$, $\mathrm{Pe_r} = 10^2$, $N = 2048$. Rod colors correspond to 2D orientation.

(a) $A = 2$, $\phi = 0.9$

(b) $A = 10$, $\phi = 0.9$

(c) $A = 2$, $\phi = 0.9$

(d) $A = 10$, $\phi = 0.9$
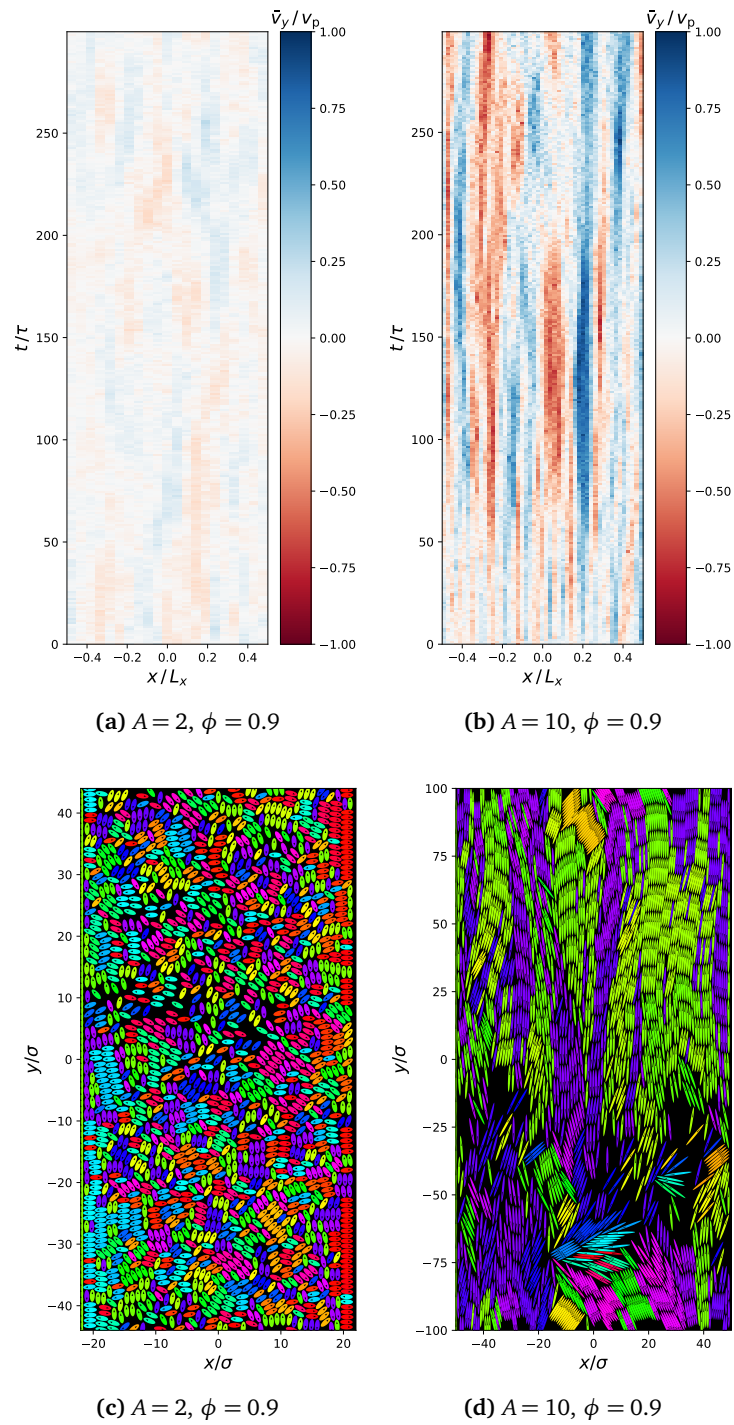
Figure 4.6: *High-density states*: Example heatmaps of the net flow profile in time **(a-b)** for individual simulations from the initial state to the $t = 300\tau$ state **(c-d)**. $\beta = 0.1$, $\mathrm{Pe_r} = 10^2$, $N = 2048$.

(a) $A = 2$, $\phi = 0.6$

(b) $A = 2$, $\phi = 0.9$

(c) $A = 4$, $\phi = 0.6$

(d) $A = 6$, $\phi = 0.6$

(e) $A = 10$, $\phi = 0.6$

(f) $A = 10$, $\phi = 0.9$
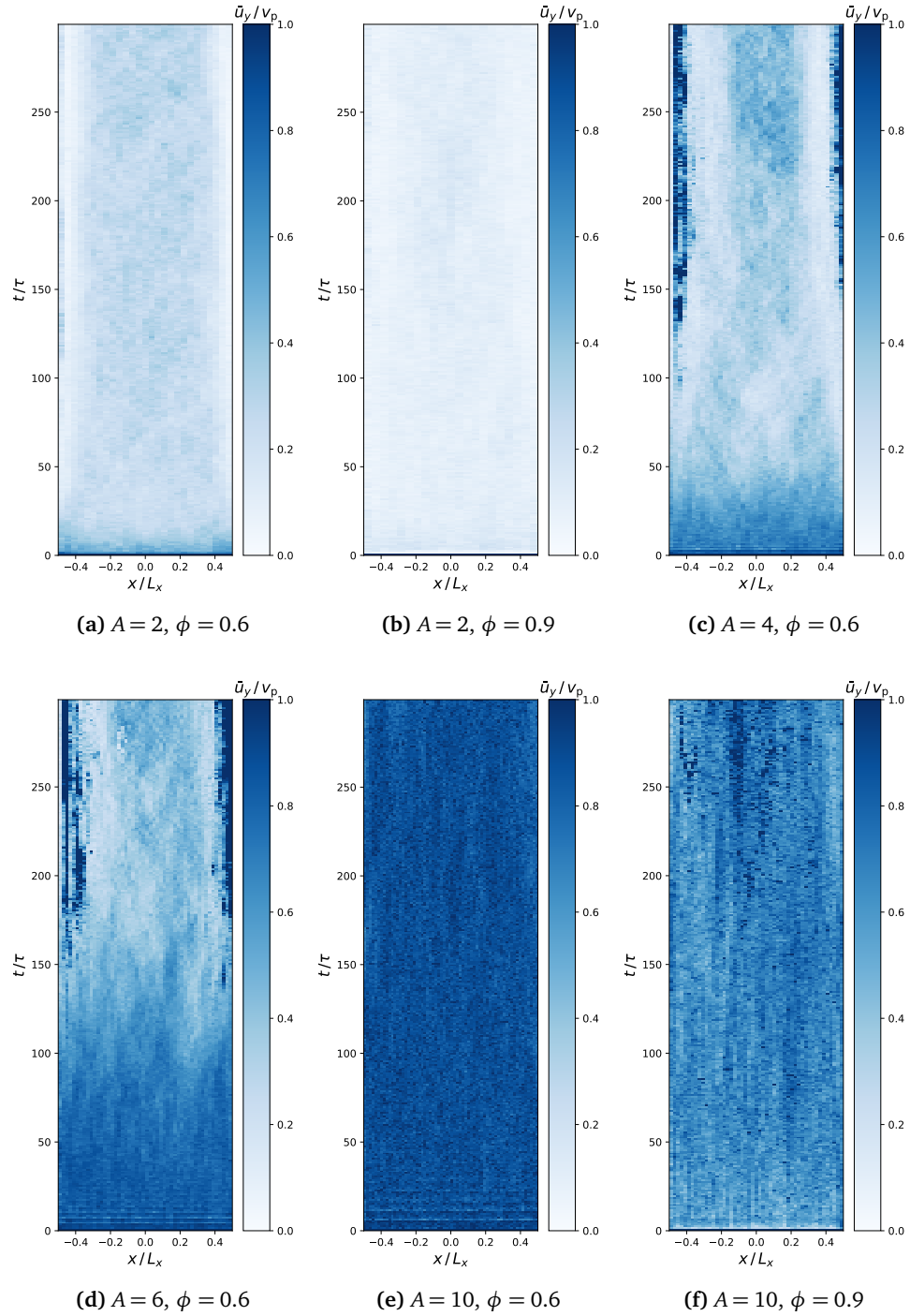
Figure 4.7: *Absolute flow profiles*: **(a-f)**: Heatmaps of the average absolute channel flow profile for three separate system realizations, from initial state to $t = 300\tau$. $\beta = 0.1$, $Pe_r = 10^2$, $N = 2048$. Darker subregions indicate areas of increased movement. The initial transient phase is characterized by a gradual slowing of the dynamics, followed by the formation of a jammed or flowing boundary layer at the barrier.

(a) $A = 2$

(b) $A = 4$

(c) $A = 6$

(d) $A = 10$
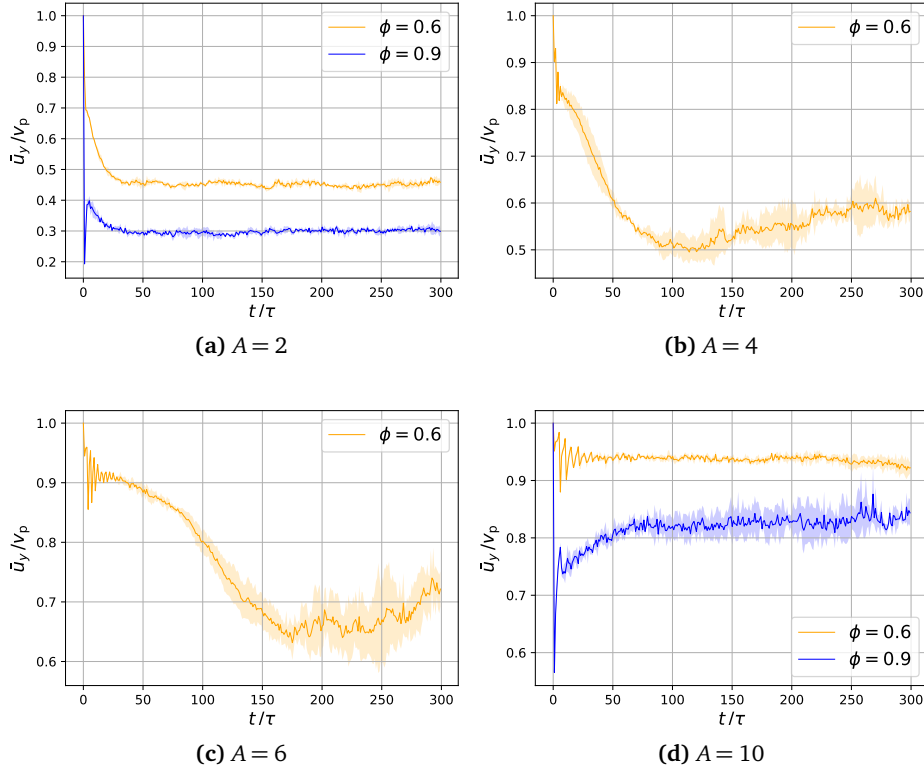
Figure 4.8: *Absolute system flow*: **(a-d)**: Average of absolute flow measurements $\bar{u}_y$ for the entire channel over time. Shaded area shows standard deviation across three individual simulations. The early oscillatory behavior is explained by the initial conditions, as the period of oscillations is close to $A\sigma/2v_p$, what we would expect from the numerous initial collision events. These are also visible as pale horizontal lines in the early absolute flow profiles in Figure 4.7.

[27]. Comparing the rod lengths and densities used in this study, the laning phase we observe is shifted towards a smaller rod aspect ratio. This may indicate that confinement to the channel forces the phase transition for shorter rods.
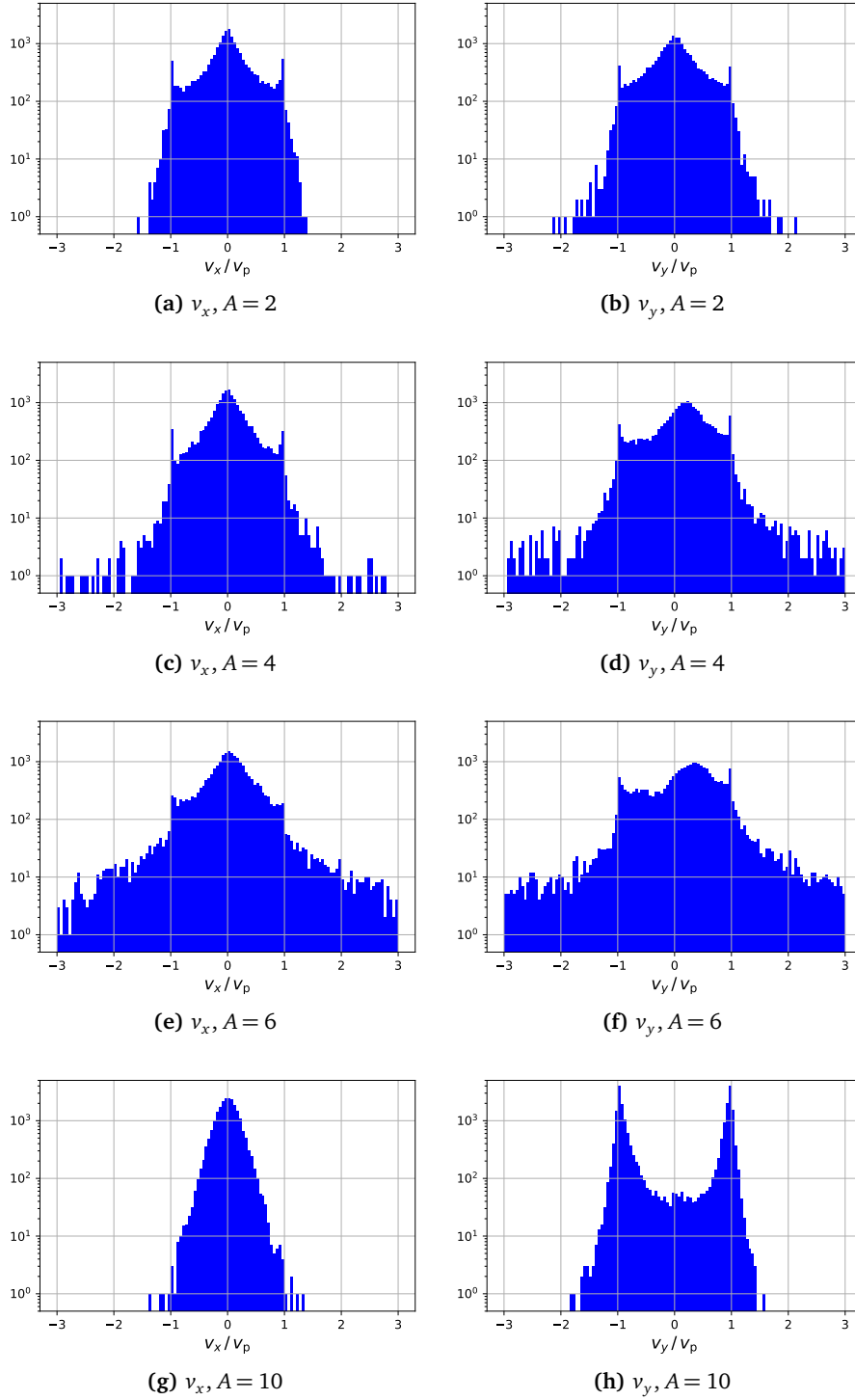
4.4.6   Velocity decomposition

The measured flow parameters give some insight into the $\hat{y}$-component of the instantaneous velocity field, which we expect to not cancel out on average, but still leaves out a few parts of the picture. To make a more in-depth investigation of the states, it will be helpful to also consider the $\hat{x}$-component of the velocity, to see whether the stagnant dynamics is a result of jamming or other effects. Additionally, the distribution of $\hat{y}$-components can help us differentiate purely horizontal motion from a zero net flow caused by averaging within subregions. Individual systems for each set of parameters A and ϕ were sampled for an additional $t = 10\tau$, while making no other changes to the system or parameters. The

distributions of the v_x, v_y velocity components are shown in Figures 4.9 and 4.10.

The distributions provide additional insight into the nature of the phases we have seen. Unsurprisingly, the v_x-components are universally symmetrical and largely concentrated around $v_x = 0$. What is more telling, is the shape of the distributions. Most of the v_x-components possess a multimodal distribution, meaning that there is a coexistence of states. A purely jammed component will have a steep non-Gaussian distribution, due to most rods being dynamically trapped. On a log-scale, this is qualitatively represented by an inverse parabola shape [53]. Peaks around $v_x = \pm v_p$ indicate a freely moving, disordered phase. Wide distributions with tails extending far beyond $|v_x| > v_p$ may at first glance seem like the result of instabilities in the first-order Euler-Maruyama method. However, these extended tails may have valid physical interpretations related to the extreme stresses within dense rod clusters. As forces build up in the densest regions, the system releases occasional "bursts" of large instantaneous movement. By the small number of rods observed in these bursts, it is indicated that these occurrences are rare and intense, likely given by a power law. The sharp central peaks and wide tails indicate the coexistence of a jammed and a characteristically turbulent regime [53]. Only the $A = 2$ and $A = 10$ systems show a distribution that can be considered close to Gaussian, explained by the relatively free gas-like $\hat{x}$-directed motion within the depletion layer and lanes, respectively.

As for the v_y-components, we see a symmetrical distribution for $A = 2, 10$, the states characterized by a symmetrical boundary layer and highly ordered laning, respectively. The systems with $A = 4, 6$ are, as mentioned, more turbulent and have skewed distributions. Due to the symmetrical initial states, this is likely the manifestation of the spontaneously excited shear flow along the wall. Frustrations within the dense boundary layers cause a wide distribution which goes beyond reasonable values. After an initial runtime of $t = 300\tau$, the $A = 10$ system has not reached a highly clustered phase, and the distribution of v_y-components is bimodal around $\pm v_p$, as we expect for nematically ordered laning.

The high-density distributions shown in Figure 4.10 show similarities to their lower-density counterparts. The major differences for short rods seems to be a taller central peak and a wider tail, likely caused by increased dynamical arrest and frustration from the repulsive forces. The distribution remains within an approximation of a Gaussian, with some rods still moving at the characteristic velocity v_p. As for long rods, the v_y-distribution shows signs of a third central peak, indicating the onset of a slowed or less ordered state. The distributions are otherwise non-Gaussian, meaning that the phases can be characterized as turbulent.

(a) v_x, $A = 2$ **(b)** v_y, $A = 2$

(c) v_x, $A = 4$ **(d)** v_y, $A = 4$

(e) v_x, $A = 6$ **(f)** v_y, $A = 6$

(g) v_x, $A = 10$ **(h)** v_y, $A = 10$

Figure 4.9: *Velocity distribution*: **(a-h)**: Log-scaled distributions of the velocity components for $\phi = 0.6$ systems with different rod aspect ratios, sampled for $t = 10\tau$ in the steady (or near-steady) state. $\beta = 0.1$, $\text{Pe}_r = 10^2$, $N = 2048$.

(a) $v_x, A = 2$

(b) $v_y, A = 2$

(c) $v_x, A = 10$

(d) $v_y, A = 10$
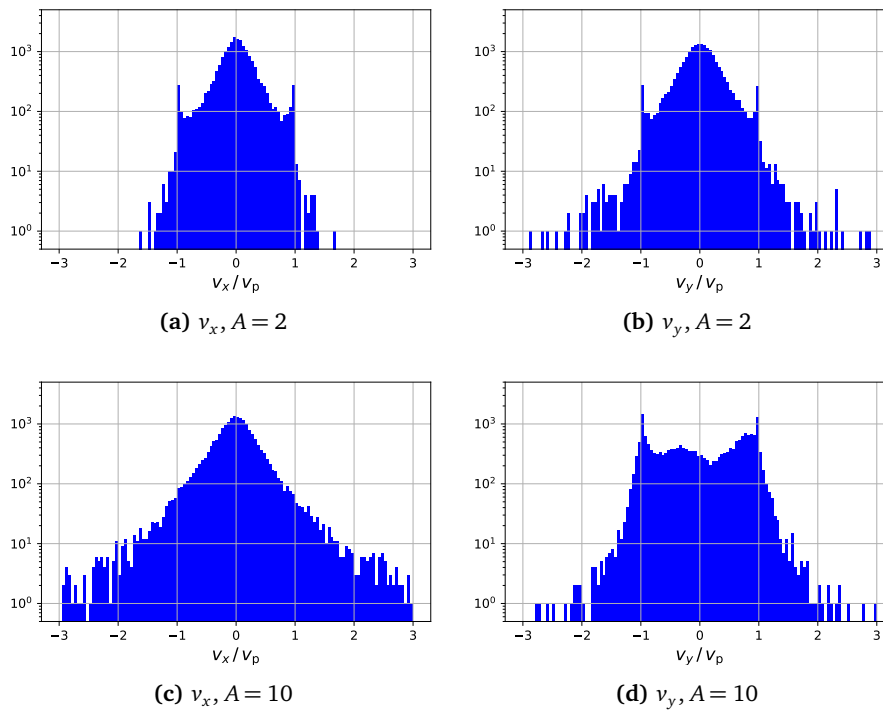
Figure 4.10: *Velocity distribution*: **(a-d)**: Log-scaled distributions of velocity components for $\phi = 0.9$ systems with different rod aspect ratios, sampled for $t = 10\tau$ in the near-steady state. $\beta = 0.1$, $\text{Pe}_r = 10^2$, $N = 2048$.

4.5 Long rods: Steady state considerations

From the measured flows and velocity distributions of the $A = 10$ systems, we cannot confirm that these systems are indeed close to a steady state. The laning phase we observed for intermediate-to-long particles generally dissolved when the initial transient behavior seized, and showed similar decreases in flow over time. The time it took for the flow to even out increases with higher values of A, and Figure 4.8(d) indicates a similar, delayed decrease. Because the $A = 10$ systems were only run for $t = 300\tau$, the maximum distance traveled for individual rods is only 30 rod lengths. We have therefore not gathered sufficient data to conclude that these systems possess a steady state characterized by laning. To more properly investigate the steady state, we continued running a single $\phi = 0.6$ and $\phi = 0.9$ system simulation for an additional $t = 900\tau$ to see if the laning behavior persisted through this extended time. The flow parameter progression and snapshots during the time interval are shown in Figures 4.11 and 4.12.
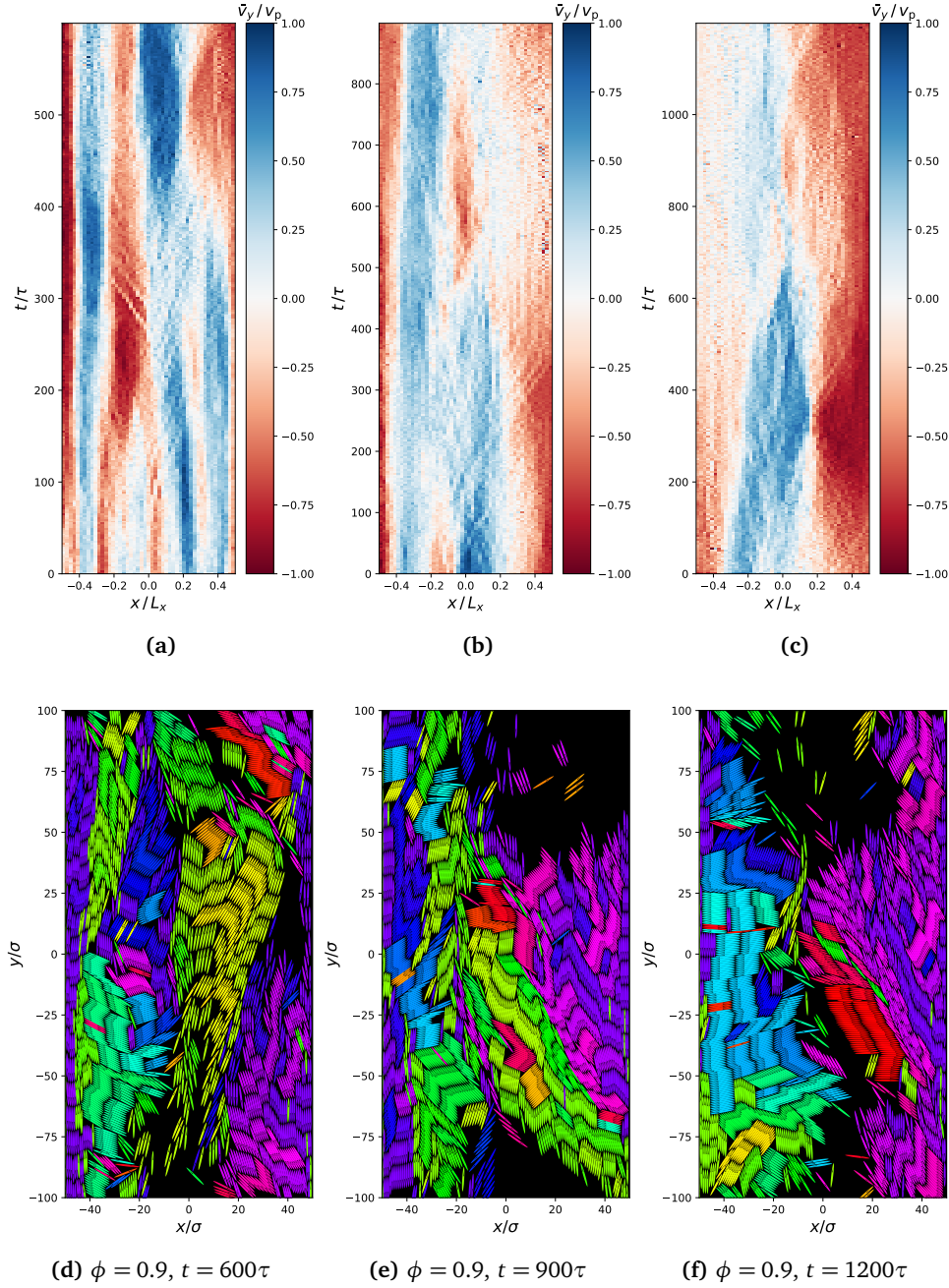
An increase in absolute flow is observed for $\phi = 0.6$, with an onset at about $t = 800\tau$. The fluctuations in the data from times beyond $t = 900\tau$ were initially deemed too extreme, and so these results are excluded from the final analysis except as visual demonstrations. As with the short-time states, the velocity components were sampled for $t = 10\tau$ after the $t = 900\tau$ states. The distributions of these components are shown in Figure 4.14.

The extended simulations strongly disagree with the previous indications that the steady state for these chosen values of A and ϕ (and the wide channel) is indeed one characterized by laning. The results instead show qualitatively that the laning is a transient behavior which eventually breaks down and creates stable structures similar to the ones described by Wensink and Löwen [47] as so-called "hedgehog-like" clusters. These occur in conjunction with a narrow wall-aligned boundary layer. After a long time $t > 900\tau$, it may be reasonable to assume that this motion will nematize the clusters and lead to a more uniform distribution of aligned rods which slide along the barrier. Moreover, the aggregation leaves a depleted region in the center similar to what is observed for other rod lengths, unlike what is expected for a laning phase. This is again supported by the individual velocity components. Wide distributions indicate highly frustrated states along the $\hat{x}$-direction from the wall aggregation. v_y-components of the $\phi = 0.6$ system does however approach a Gaussian as a result of the released shear flow. At these times, it is demonstrated that the behavior of long rods is characteristically similar to the $A = 4, 6$ lengths.

(a) **(b)** **(c)**

(d) $\phi = 0.6$, $t = 600\tau$ **(e)** $\phi = 0.6$, $t = 900\tau$ **(f)** $\phi = 0.6$, $t = 1200\tau$
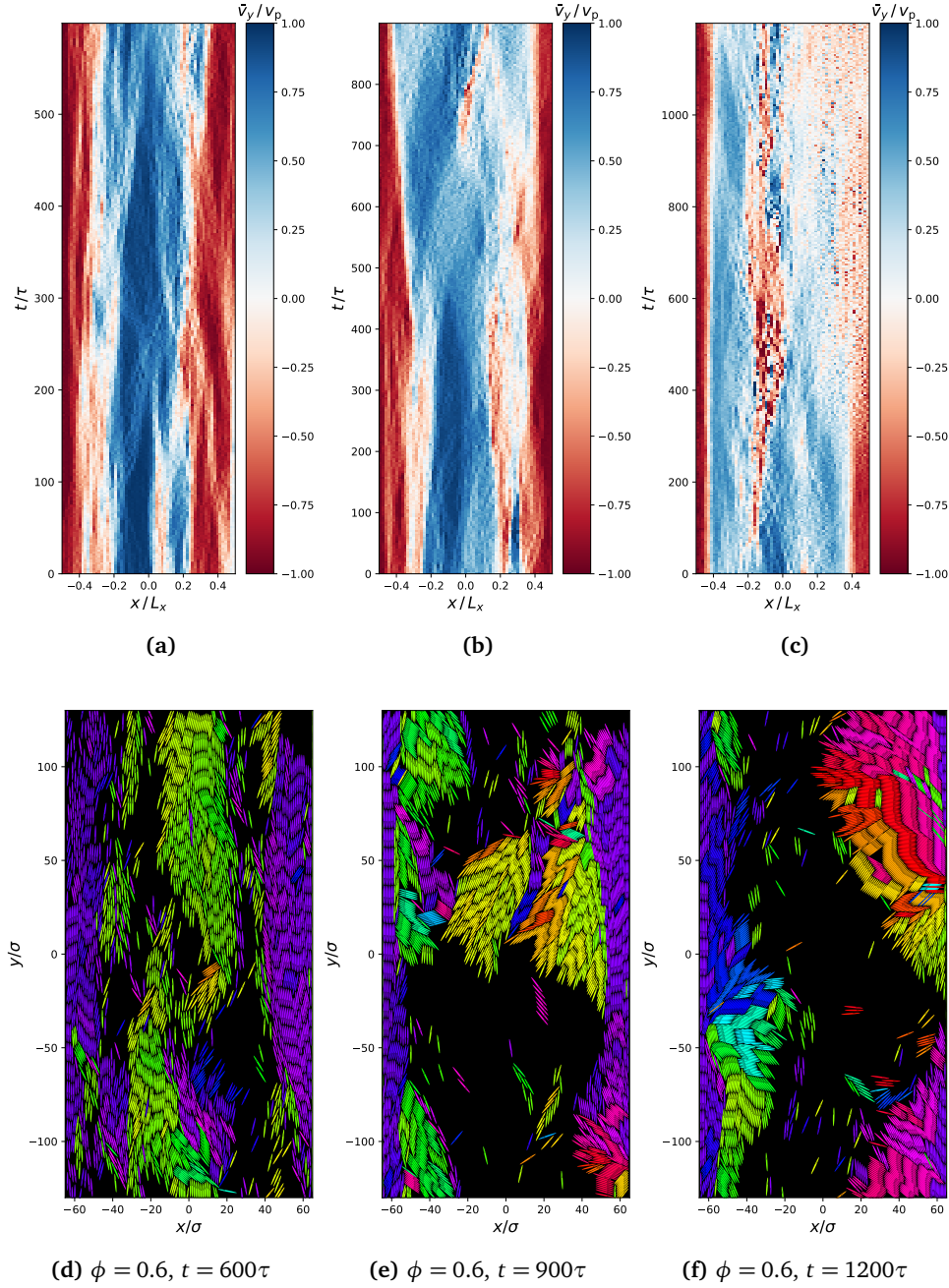
Figure 4.11: *Extended runs*: **(a-c)**: Net flow profile evolution in each 300τ time interval. **(d-f)**: State snapshots. $A = 10$, $\beta = 0.1$, $\mathrm{Pe_r} = 10^2$, $N = 2048$.

(a)　　　　　　　**(b)**　　　　　　　**(c)**

(d) $\phi = 0.9$, $t = 600\tau$　　　**(e)** $\phi = 0.9$, $t = 900\tau$　　　**(f)** $\phi = 0.9$, $t = 1200\tau$
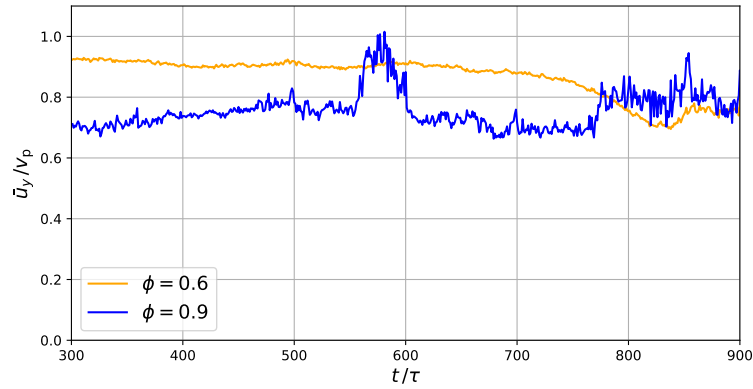
Figure 4.12: *Extended runs*: **(a-c)**: Net flow profile evolution in each 300τ time interval. **(d-f)**: State snapshots. $A = 10$, $\beta = 0.1$, $\mathrm{Pe_r} = 10^2$, $N = 2048$.

Figure 4.13: *Decreasing flow*: Absolute system-averaged flow parameter measurements for the individual extended $A = 10$ simulations. $\beta = 0.1$, $Pe_r = 10^2$. Large magnitudes and fluctuations come as the result of compression along the channel walls.

(a) v_x, $\phi = 0.6$

(b) v_y, $\phi = 0.6$

(c) v_x, $\phi = 0.9$

(d) v_y, $\phi = 0.9$
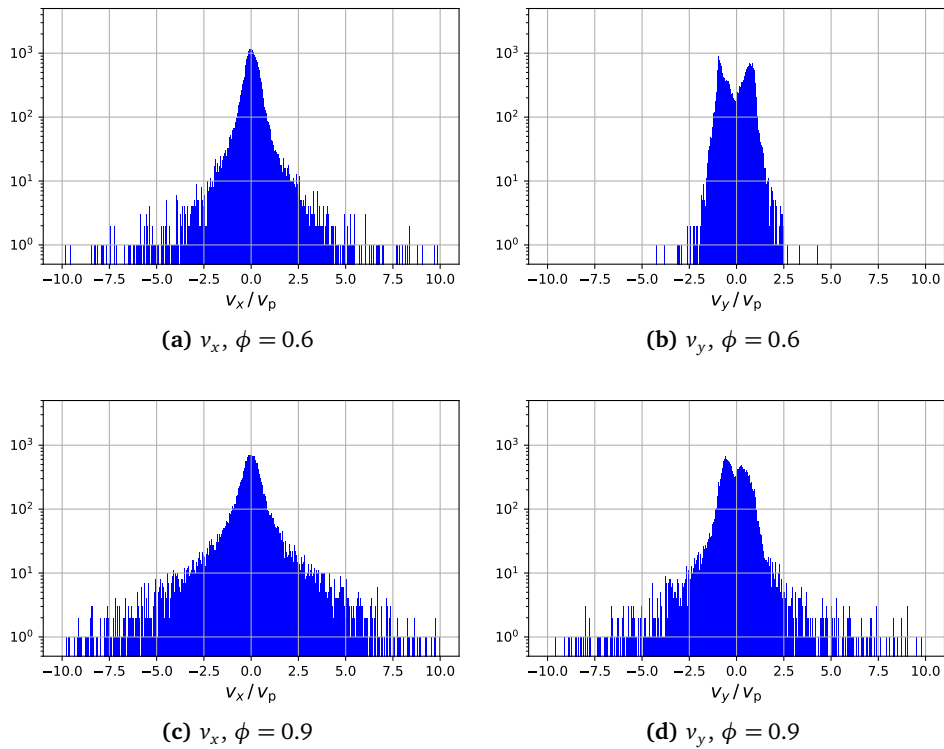
Figure 4.14: *Velocity distribution*: **(a-d)**: Distributions of velocity component magnitudes sampled for $t = 10\tau$ after a total evolution time $t = 900\tau$.
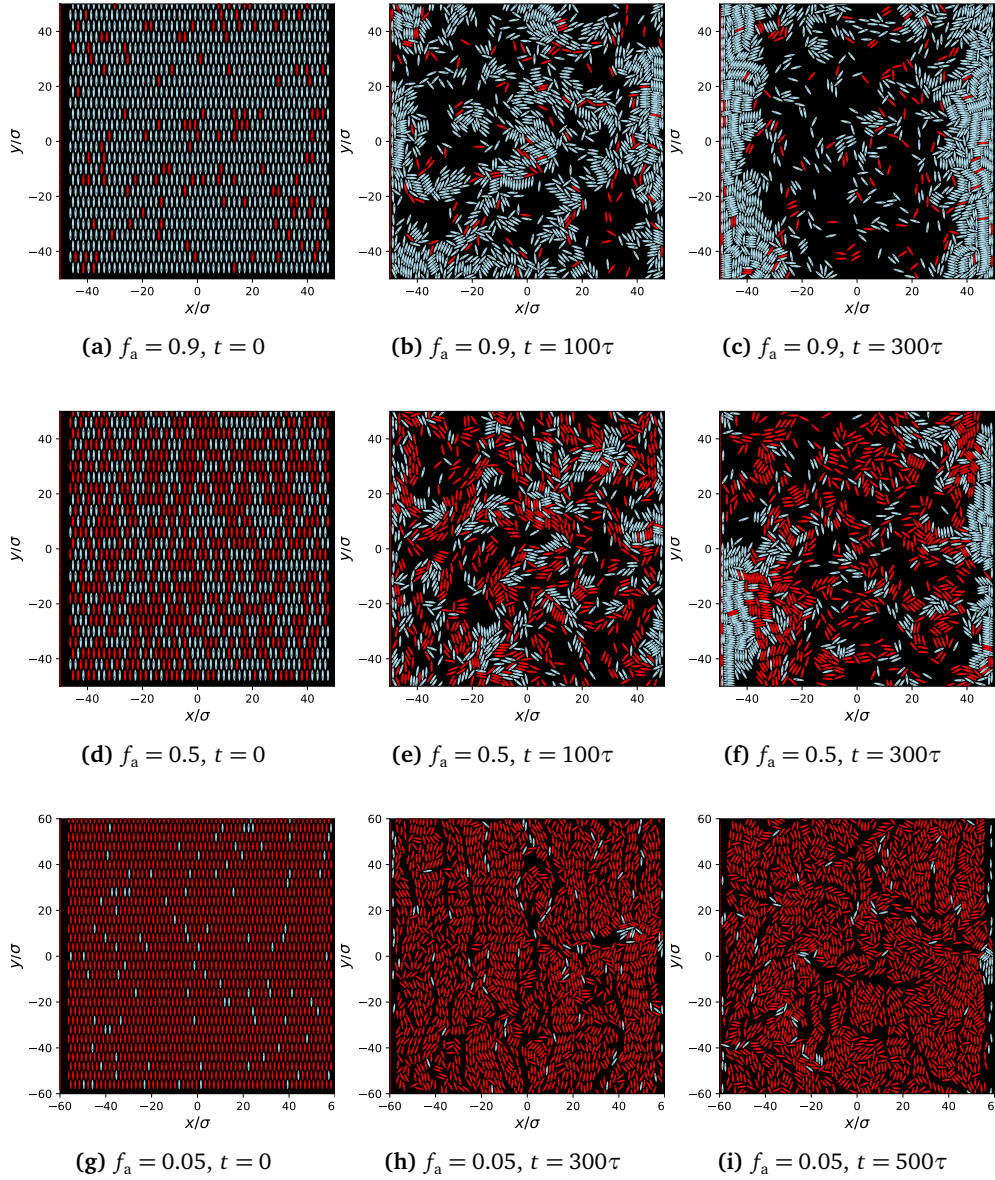
4.6   Partially motile systems

As observed and discussed in previous sections, the active systems we investigate show a high degree of clustering and ordering. Because every particle moves with the same motility, large structures of several particles form spontaneously, combine with other clusters or disintegrate due to noise or collisions. This behavior might in many ways seem idealized or unrealistic if seen from a biological perspective. In nature, individual specimens of a specific life-form may exhibit large variations in behavior, size, speed and consistency in all of the above. Focusing specifically on speed, models of polydisperse systems of self-propelled particles have have been studied in an effort to describe behavior observed in nature. Among them is an observed phase separation of active liquid crystal particles with different motilities [4] and spontaneous segregation in mixtures of active and passive polar rods. The main inspiration for the latter is to study how the dynamics of the systems change when some portion is assumed dead or otherwise non-motile, a case encountered in bacterial colonies [33].

As a matter of curiosity then, we qualitatively investigate systems within the same channel boundary conditions, where only a fraction f_a of the particles experience self-phoretic motion. The binary $v_{p,i} \in \{0, v_p\}$ scenario is of most practical interest, as we do not need to make any statements about the distribution of the self-propulsion velocities other than the fraction f_a. We choose to simulate rods with aspect ratio $A = 4$, as this is within the range values of high microbiological relevancy. Systems of density $\phi = 0.48$ with three different motile fractions were run for typical time intervals with low noise and moderate repulsion strength. Snapshots of the initial, final and intermediate states are shown in Figure 4.15. Another higher-density system was run for a longer time interval to see if the increased collision frequency induced a more segregated state. Snapshots are shown in Figure 4.16.
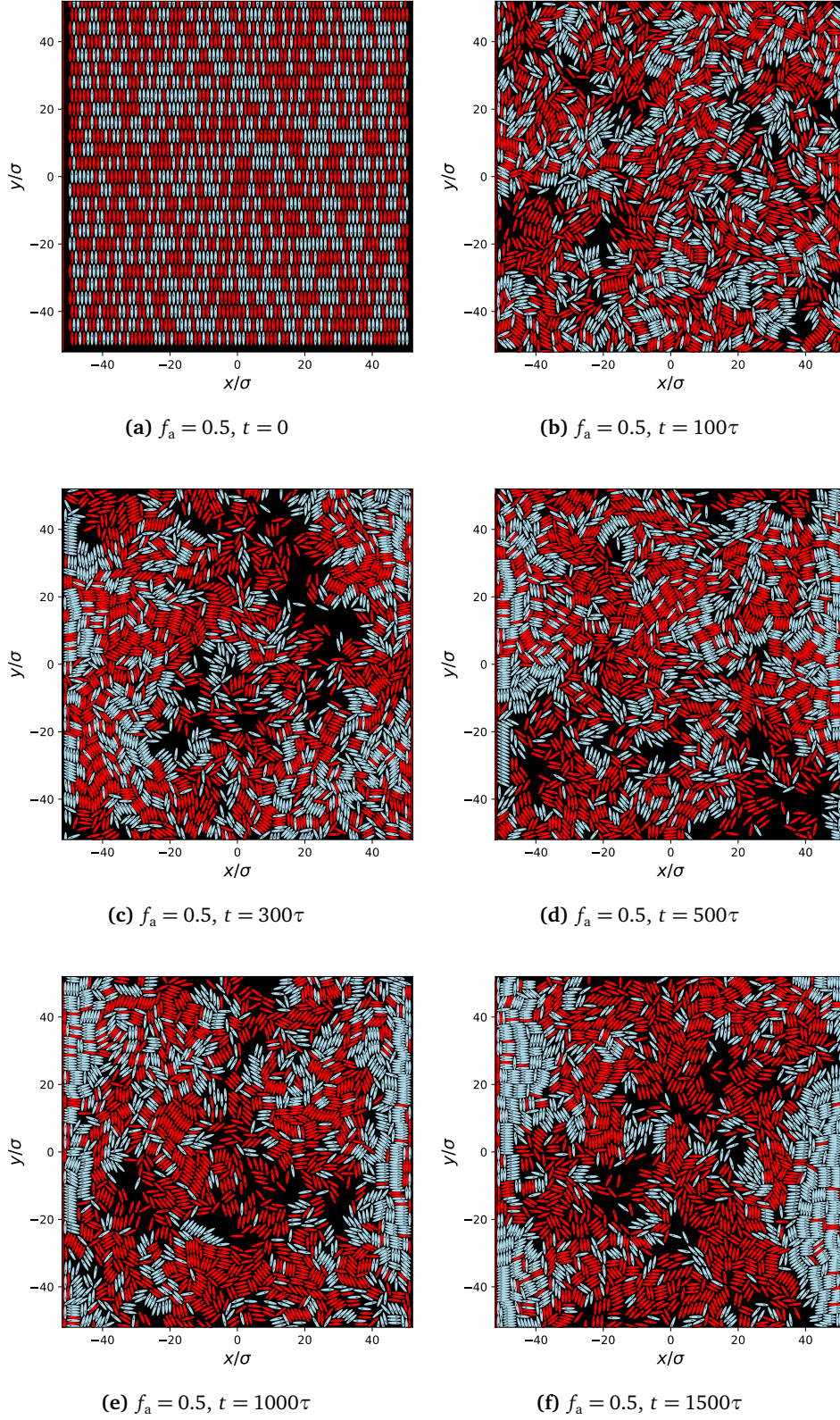
4.6.1   Exotic phase separation

The evolution of the moderate-density systems in Figure 4.15 shows similar behavior to the systems of uniform motility in Section 4.4, due to having a significant fraction of active rods. However, a visible segregation of active and passive rods occurs not long after the systems are set in motion. Subfigures 4.15(a-c) show that the active rods migrate and create dense regions close to the barrier on either side, while passive rods are left in a largely unchanged uniform distribution. The relatively low density allows active particles to bypass most of the passive obstacles, although some passive rods may be carried outward for some distance and trapped within the active clusters. This is a scenario described as an *active bath*, where passive particles subject to the non-thermal fluctuations from the surrounding active particles tend to experience superdiffusive motion like their active counterparts [6].

Systems of similar numbers of passive and active particles in Subfigures 4.15(d-

Figure 4.15: *Mixed systems*: **(a-i)**: Snapshots for partially motile $A = 4$ systems in a $\hat{y}$-directed channel. Active rods are shown in cyan, passive rods in red. $\phi = 0.48$, $\mathrm{Pe_r} = 10^3$, $\beta = 0.1$. Total particle numbers $N = 1300, 1300, 1800$, respectively.

(a) $f_a = 0.5$, $t = 0$

(b) $f_a = 0.5$, $t = 100\tau$

(c) $f_a = 0.5$, $t = 300\tau$

(d) $f_a = 0.5$, $t = 500\tau$

(e) $f_a = 0.5$, $t = 1000\tau$

(f) $f_a = 0.5$, $t = 1500\tau$

Figure 4.16: *High-density mixture*: **(a-f)**: Snapshots of the evolution of partially motile $A = 4$ system in a channel. Active rods are shown in cyan, passive rods in red. $\phi = 0.80$, $Pe_r = 10^3$, $\beta = 0.1$. Total particle number $N = 2200$.

f) show a distinct phase separation, possibly resulting in a complete separation in the long time limit. Overall, the distribution of passive particles appears to get narrower as active particles aggregate at the barrier. Rods collect at the barrier symmetrically (the distribution is mirrored in $x = 0$), which is what we would expect with both noise and initial positions having no preferential direction.

The low-motile fraction case in Subfigures 4.15(g-i) show another type of characteristics. The few randomly distributed active particles may be seen as contained in a crowd of passive rods, an exaggerated analogy of the medium in which the rods themselves are immersed. This has been dubbed called *active doping,* and have been shown to cause a "herding" behavior, resulting in a state of passive rods gathered in flocks by external compression [6]. We see the onset of such a state, mainly caused by the vacant trails left behind by the active rods. Quite interestingly, the active rods cut through the dense environment and eventually gather in small clusters. This is likely due to following the already-cleared paths created by other active rods, where lower density and reflection from the path walls allows for faster movement. In a sense, this effective hydrodynamic interaction is a long-range effect of short-range repulsion. The active clusters ultimately gather at the barrier when one is encountered, much like in the other scenarios, likely causing complete separation after long times.

As one would expect, the evolution of the high-density system shown in Figure 4.16 exhibits slower changes in time. This is likely due to the active rods having a much harder time getting past the crowd of passive rods, causing jammed regions and redirecting rods back into the center of the channel. By visual inspection, however, we see that the separation of active and passive rods is similar to the low-density scenario, and will probably segregate in the same way in the long time limit. Higher noise might cause the aggregated regions to partly dissolve, creating a steady state mixture in the center of the channel and thus a more even density profile for the entire channel width.

Chapter 5

Discussion

5.1 ABR simulations: Conclusion

The previous Chapter presented the results obtained from simulations of a hybrid ABR model, as well as some discussion of our observations. From these observations, we can make general statements about the properties of our model. The line segment model tends to order in a smectic phase at high density, not unlike what is observed for rigid polymer models [33]. This manifests in clustering behavior which is characterized by long correlated bands.

By confining the active system to a channel, behavior changes from the case of simple periodic boundary conditions. We observe qualitatively different near-steady state behavior for systems of different rod aspect ratios A, as well as different equal-time states for system with different effect area fractions ϕ. Higher-density systems generally possess slowed dynamics and longer relaxation times. The most prominent feature is the formation of a boundary layer which goes from a preferential direction perpendicular to the barrier for short rod lengths to alignment parallel to it for long rods. In the intermediate rod length regime, there seems to be a continuous coexistence. This transitions influences the instantaneous flow through the channel, with longer rods seemly allowing for large shear flows along the channel walls, while short rods stagnate due to jamming. The aggregation-phenomenon along barrier is robust with regard to partially active systems, with active particles collecting at the walls in both high-density and low-active fraction regimes.

Longer rods possess the potential for stratified lane formation, but we suspect that a steady state will be highly dependent on the initial conditions of the system. We initialize a perfect nematic arrangement of rods with a 50-50 $\pm \hat{y}$ distribution of orientations. Because of this, we would expect that the emerging lanes have a nearly identical distribution, given that the density is high enough to prevent frequent rod reorientations. In future models, varying the ratio of the oppositely oriented rods may have a biological significance. A rigorous evaluation might uncover regimes of higher or lower net flows, a higher or lower number of lanes, or even a completely polarized steady state.

(a) Results adapted from [27].

(b) Results from our experiments.
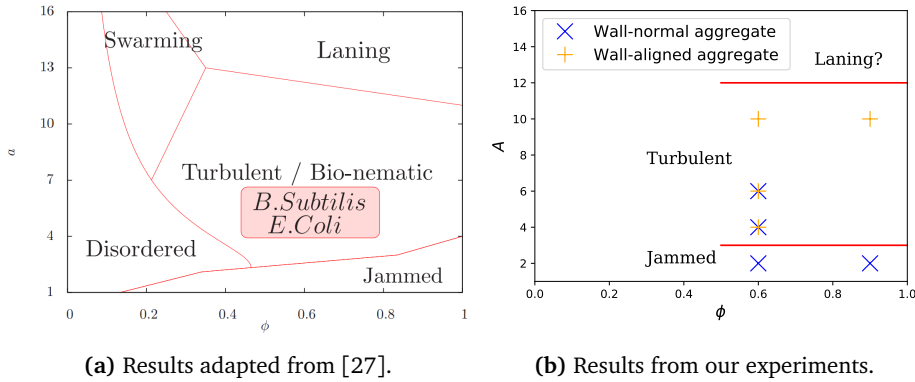
Figure 5.1: *ABR steady states*: **(a)**: Phase diagram showing the observed steady states of n-mer ABRs in periodic boundary conditions with varying packing fraction ϕ and rod aspect ratio a. **(b)**: Summary of the phase behavior observed for our rod model in a periodic channel.

We can summarize the observed phase behavior in the diagram shown in Figure 5.1(b). When compared to the phase diagram by Wensink and Löwen [27], the observed behavior is in agreement. However, we can make a different type of differentiation in terms of the way rods aggregate at the walls, either by ordering along the wall, into the wall or as a mix. It is possible that influence from the channel wall can shift the phase transitions and have a larger impact on system order and flow than what we observed in our experiments. We can imagine that the inclusion of a parameter to relate the channel size and rod parameters will allow a shift of the phases, e.g. by restricting rotation of long rods to produce stable lane formation for rods of shorter lengths or lower densities.

5.2 Methods

5.2.1 Model parameters

One of the most challenging aspects of active matter research is to be able to make general statements from complex systems with a large amount of parameters. To narrow the available parameter space, it is worthwhile to understand the individual model's dependency on certain parameters. In this regard, the repulsive potential has not been given an extensive analysis. As this feature plays an important role both in relation to the self-propulsion force F_p and the effective area fraction ϕ, the potential height β may have an unknown and likely significant effect on the dynamics. The 6-3 modified Weeks-Chandler-Anderson is a variation of one of several common soft potentials, and this is a choice left largely to the individual. In the work for this thesis, a steeper 12-6 WCA-potential was deemed too steep to allow for stable simulations of long rods. Further improvements in stability could have been made by having the repulsive force be differentiable at the cut-off radius, $\partial_r F_{rep} = 0$ for an even softer force. This could, however, lead

to increased over-compression of systems, allowing for higher values of $\phi > 1$.

Another example is one mentioned by Wensink and Löwen: making a rigorous consideration of the rotational noise. This might have even greater significance while investigating the effect of bounded systems, as it relates directly to the effective system size. Nonetheless, it could potentially show how increased noise influences the relaxation times for the steady states, be it by dismantling ordered regions or by causing increased dynamical arrest.

5.2.2 Determining steady state

The introduction of a channel poses issues with regard to determining a steady state under certain circumstances. In active matter systems, the steady state may be assumed by the convergence of a probability distribution. This is opposed to equilibrium matter, where the steady state may be characterized from various other parameters, including order parameters. The coexistence of states caused by the barriers makes it challenging to properly determine the prominence of each one. In retrospect, it would have been useful to measure the *surface excess*, which can aid in quantifying the wall aggregation [35].

We suspect that the steady state of medium- to high-density long rod systems may be highly dependent on initial conditions in the relatively short time intervals we have examined. We would have ideally wanted to simulate systems for times far beyond what was shown in this work. As an example, Wensink and Löwen [27] relax the system for $t = 10^3 \tau$ before entering the measurement phase of the simulations. For these times to be reasonable for the system sizes and interactions we consider here, additional work is required in terms of stabilizing the algorithm and use better suited hardware resources. Furthermore, because of the suppression of rotational motion, there will be less frequent complete rod reorientations with respect to the channel. In this case, the distribution of rod orientations, as well as the number of lanes may be conserved in the steady state. If we were to investigate this further, we could quantify the amount of rod reorientations occurring in the system. Deliberately varying the channel width may allow us to characterize the phase behavior by its relationship to rod dimensions and the persistence number.

Moreover, it would have been useful to quantify the order of the emergent rod configurations, e. g. by introducing a smectic order parameter to measure the width of formed bands. This behavior is central to the clustering behavior of rods with the specific geometrical properties we chose for our ABR systems. Because the rod aspect ratio can be regarded as the effective alignment strength, we could relate this value to the rotational noise and made further investigations into the formation of bands, and any collective band dynamics.

5.2.3 Numeric considerations

The method used to calculate the interparticle interaction distance is not ideal. Our model of rigid rods assumes that the interaction strength and point of action is determined by the closest point of two rods. This should be refined to instead

account for the complete area of overlap in order to distribute the repulsive force in a more realistic way. The second assumption of this algorithm is that one of the two contact points between two rods is an end-point of one rod. This is a massive time save in the short term, although it comes with a disadvantage due to a feature of this spherocylinder rod geometry, namely its smectic-nematic ordering scheme. As rods collect in wide bands, the rotational forces always act as a shear on the band, possibly being amplified in a "domino"-like chain of torque mediation. This, along with the discontinuous derivative of the repulsive force, can allow small perturbations to cause large numerical instabilities, and thus shorter time steps are needed for systems of longer rods.

5.3   Outlook

The model of self-propelled rods we have investigated is quite flexible in terms of adding additional complexity in the form of new exotic interactions and boundary conditions. While aiming to gain understanding of the physics of living beings, the natural step would be to extend the model to fit to the parameters of known biological systems.

Perhaps one of the most useful and physically relevant improvements would be to generalize the model into 3D. In the study of active matter, systems are most commonly confined to 2D or quasi-2D, where rods are allowed to rotate into the third dimension [4]. Taking the 2D channel and creating a smooth cylindrical (topologically toroidal) boundary may combine previous knowledge the flow profile along the tube, as well as the confined dynamics in each cross-section. Moreover, by the inclusion of polydispersion of size and motility, as well as passive obstacles, this could be of high relevance in a microbiological or medical context.

Bibliography

[1]   M. Kleman and O. D. Lavrentovich. *Soft Matter Physics: An Introduction*. New York: Springer, 2003. ISBN: 978-0-387-95267-3.

[2]   L. Berthier and J. Kurchan. *Lectures on non-equilibrium active systems*. 2018. eprint: 1906.04039.

[3]   M. C. Marchetti, J. F. Joanny, S. Ramaswamy, T. B. Liverpool, J. Prost, M. Rao and R. A. Simha. 'Hydrodynamics of soft active matter'. In: *Rev. Mod. Phys.* 85 (2013), pp. 1143–1189. DOI: 10.1103/RevModPhys.85.1143. URL: https://link.aps.org/doi/10.1103/RevModPhys.85.1143.

[4]   O. J. Meacock, A. Doostmohammadi, K. R. Foster et al. 'Bacteria solve the problem of crowding by moving slowly'. In: *Nat. Phys* 17 (2021), pp. 205–210. DOI: 10.1038/s41567-020-01070-6. URL: https://doi.org/10.1038/s41567-020-01070-6.

[5]   F. Schweitzer. *Brownian Agents and Active Particles*. Berlin: Springer, 2003. ISBN: 978-3-540-73844-2.

[6]   C. Bechinger, R. Leonardo, H. Lowen, C. Reichhardt and G. Volpe. 'Active Particles in Complex and Crowded Environments'. In: *Rev. Mod. Phys.* 88 (2016), p. 045006.

[7]   X.-Q. Shi and Y.-Q. Ma. 'Topological structure dynamics revealing collective evolution in active nematics'. In: *Nat. Commun* 4 (2013), p. 3013. DOI: 10.1038/ncomms4013. URL: https://doi.org/10.1038/ncomms4013.

[8]   Y. Yang, N. Jamilpur, B. Yao et al. 'Probing Leader Cells in Endothelial Collective Migration by Plasma Lithography Geometric Confinement'. In: *Sci. Rep.* 6 (2016), p. 22707. DOI: https://doi.org/10.1038/srep22707. URL: https://www.nature.com/articles/srep22707.

[9]   O. Biham, A. A. Middleton and D. Levine. 'Self-organization and a dynamical transition in traffic-flow models'. In: *Phys. Rev. A* 46.10 (1992), p. 46. DOI: 10.1103/PhysRevA.46.R6124. URL: https://arxiv.org/abs/cond-mat/9206001.

[10]   D. Helbing, A. Johansson and H. Z. Al-Abideen. 'Dynamics of crowd disasters: An empirical study'. In: *Phys. Rev. E* 75 (2007). DOI: 10.1103/PhysRevE.75.046109. URL: https://link.aps.org/doi/10.1103/PhysRevE.75.046109.

[11]   T. E. Angelini, E. Hannezo, X. Trepat, M. Marquez, J. J. Fredberg and D. A. Weitz. 'Glass-like dynamics of collective cell migration'. In: *Proc. Natl. Acad. Sci. U.S.A.* 108.12 (2011), pp. 4714–4719. ISSN: 0027-8424. DOI: `10.1073/pnas.1010059108`. URL: `https://www.pnas.org/content/108/12/4714`.

[12]   J. Deseigne, O. Dauchot and H. Chaté. 'Collective Motion of Vibrated Polar Disks'. In: *Phys. Rev. Lett.* 105 (2010), p. 098001. DOI: `10.1103/PhysRevLett.105.098001`. URL: `https://arxiv.org/abs/1004.1499`.

[13]   M. P. Marder. *Condensed Matter Physics, 2nd Edition*. Wiley, 2015. ISBN: 978-0-470-61798-4.

[14]   É. Fodor and M. C. Marchetti. 'The statistical physics of active matter: From self-catalytic colloids to living cells'. In: *Physica A: Statistical Mechanics and its Applications* 504 (2018), pp. 106–120. ISSN: 0378-4371. DOI: `10.1016/j.physa.2017.12.137`. URL: `http://dx.doi.org/10.1016/j.physa.2017.12.137`.

[15]   K. Kruse, Joanny J.F., F. Jülicher, J. Prost and K. Sekimoto. 'Asters, Vortices, and Rotating Spirals in Active Gels of Polar Filaments'. In: *Phys. Rev. Lett.* 93 (2004), p. 078101. DOI: `10.1103/PhysRevLett.92.078101`. URL: `https://link.aps.org/doi/10.1103/PhysRevLett.92.078101`.

[16]   A. Doostmohammadi, J. Ingés-Mullol, J. M. Yeomans et al. 'Active Nematics'. In: *Nat. Commun.* 9 (2018), p. 3246. DOI: `10.1038/s41467-018-05666-8`. URL: `https://doi.org/10.1038/s41467-018-05666-8`.

[17]   L. Giomi, M. Bowick, P. Mishra, R. Sknepnek and M. C. Marchetti. 'Defect dynamics in active nematics'. In: *Phil. Trans. Series A* 372 (2014). DOI: `10.1098/rsta.2013.0365`.

[18]   G. Duclos, C. Blanch-Mercader, V. Yashunsky et al. 'Spontaneous shear flow in confined cellular nematics'. In: *Nat. Phys.* 14 (2018), pp. 728–732. DOI: `10.1038/s41567-018-0099-7`. URL: `https://doi.org/10.1038/s41567-018-0099-7`.

[19]   T. Vicsek et al. 'Novel type of phase transition in a system of self-driven particles'. In: *Phys. Rev. Lett.* 75.6 (1995), pp. 1226–1229. DOI: `10.1103/PhysRevLett.75.1226`. URL: `https://link.aps.org/doi/10.1103/PhysRevLett.75.1226`.

[20]   G. Grégoire and H. Chaté. 'Onset of Collective and Cohesive Motion'. In: *Phys. Rev. Lett.* 92 (2004), p. 025702. DOI: `10.1103/PhysRevLett.92.025702`. URL: `https://link.aps.org/doi/10.1103/PhysRevLett.92.025702`.

[21]   E. M. Purcell. 'Life at low Reynolds number'. In: *Am. J. Phys.* 45.3 (1977). DOI: `10.1119/1.10903`. URL: `https://aapt.scitation.org/doi/10.1119/1.10903`.

[22]   P. Langevin. 'Sur la théorie du mouvement brownien'. In: *C. R. Acad. Sci. (Paris)* 146 (1908), pp. 530–533.

[23] R. M. Navarro and S. M. Fielding. 'Clustering and phase behaviour of at-
      tractive active particles with hydrodynamics'. In: *Soft Matter* 11 (2015),
      p. 7525. DOI: 10.1039/C5SM01061F. URL: https://pubs.rsc.org/en/
      content/articlelanding/2015/SM/C5SM01061F#!divAbstract.

[24] J. R. Howse, R. A. L. Jones, A. J. Ryan, T. Gough, R. Vafabakhsh and R.
      Golestanian. 'Self-Motile Colloidal Particles: From Directed Propulsion to
      Random Walk'. In: *Phys. Rev. Lett.* 99 (2007), p. 048102. DOI: 10.1103/
      PhysRevLett.99.048102. URL: https://link.aps.org/doi/10.1103/
      PhysRevLett.99.048102.

[25] M. E. Cates and J. Tailleur. 'When are active Brownian particles and run-
      and-tumble particles equivalent? Consequences for motility-induced phase
      separation'. In: *Eur. Phys. Lett.* 101.2 (2013). DOI: 10.1209/0295-5075/
      101/20010. URL: https://iopscience.iop.org/article/10.1209/0295-
      5075/101/20010/meta.

[26] D. Grossman, I. S. Aranson and E. Ben Jacob. 'Emergence of agent swarm
      migration and vortex formation through inelastic collisions'. In: *New J.
      Phys.* 10.2 (2008), p. 023036. DOI: 10.1088/1367-2630/10/2/023036.
      URL: https://doi.org/10.1088%5C%2F1367-2630%5C%2F10%5C%2F2%5C%
      2F023036.

[27] H. H. Wensink and H. Löwen. 'Emergent states in dense systems of act-
      ive rods: from swarming to turbulence'. In: *J. Phys.: Condens. Matter* 24
      (2012), p. 464130. DOI: 10.1088/0953-8984/24/46/464130. URL: https:
      //arxiv.org/abs/1204.0381.

[28] J. E. Lennard-Jones. 'On the determination of molecular fields.—I. From
      the variation of the viscosity of a gas with temperature'. In: *Proc. R. Soc.
      Lond.* 106 (1924), pp. 441–462. URL: https://doi.org/10.1098/rspa.
      1924.0081.

[29] J. D. Weeks, D. Chandler and H. C. Andersen. 'Role of Repulsive Forces
      in Determining the Equilibrium Structure of Simple Liquids'. In: *J. Chem.
      Phys.* 54.12 (1971), p. 5237. DOI: 10.1063/1.1674820. URL: https://doi.
      org/10.1063/1.1674820.

[30] A. Zöttl and H. Stark. 'Emergent behavior in active colloids'. In: *Phys.: Con-
      dens. Matter* 28 (2016). DOI: 10.1103/PhysRevE.75.046109. URL: https:
      //doi.org/10.1088/0953-8984/28/25/253001.

[31] J. Olafsen. *Experimental and Computational Techniques in Soft Condensed
      Matter Physics*. Cambridge: Cambridge University Press, 2010. ISBN: 978-
      0-511-76054-9.

[32] M. Abkenar, K. Marx, T. Auth and G. Gompper. 'Collective behavior of pen-
      etrable self-propelled rods in two dimensions'. In: *Phys. Rev. E* 88 (2013),
      p. 062314. DOI: 10.1103/PhysRevE.88.062314. URL: https://link.aps.
      org/doi/10.1103/PhysRevE.88.062314.

[33] S. R. McCandlish, A. Baskaran and M. F. Hagan. 'Spontaneous segregation of self-propelled particles with different motilities'. In: *Soft Matter* 8 (2012), pp. 2527–2534. DOI: 10.1039/C2SM06960A. URL: https://pubs.rsc.org/en/content/articlelanding/2012/SM/c2sm06960a#!divAbstract.

[34] E. Gauger. 'Hydrodynamics of nanomachines in biology'. In: (2005). URL: https://www.researchgate.net/publication/30017028_Hydrodynamics_of_nanomachines_in_biology.

[35] J. Elgeti and G. Gompper. 'Wall accumulation of self-propelled spheres'. In: *Eur. Phys. Lett.* 101.4 (2013), p. 48003. DOI: 10.1209/0295-5075/101/48003. URL: https://doi.org/10.1209/0295-5075/101/48003.

[36] C. Vega and S. Lago. 'A fast algorithm to evaluate the shortest distance between rods'. In: *Computers Chemistry* 18.1 (1994), pp. 55–59. DOI: 10.1016/0097-8485(94)80023-5. URL: https://www.sciencedirect.com/science/article/pii/0097848594800235.

[37] A. P. Solon, Y. Fily, A. Baskaran, M. E. Cates, Y. Kafri, M. Kardar and J. Tailleur. 'Pressure is not a state function for generic active fluids'. In: *Nat. Phys.* 11.8 (2015), pp. 673–678. ISSN: 1745-2481. DOI: 10.1038/nphys3377. URL: http://dx.doi.org/10.1038/nphys3377.

[38] Y. Yang, V. Marceau and G. Gompper. 'Swarm behavior of self-propelled rods and swimming flagella'. In: *Phys. Rev. E* 82 (2010), p. 031904. DOI: 10.1103/PhysRevE.82.031904. URL: https://link.aps.org/doi/10.1103/PhysRevE.82.031904.

[39] H. Ikeda, C. Brito and M. Wyart. 'Infinitesimal asphericity changes the universality of the jamming transition'. In: *J. Stat. Mech.: Theory Exp.* 2020.3 (2020), p. 033302. ISSN: 1742-5468. DOI: 10.1088/1742-5468/ab74cb. URL: http://dx.doi.org/10.1088/1742-5468/ab74cb.

[40] V. Narayan, S. Ramaswamy and N. Menon. 'Long-Lived Giant Number Fluctuations in a Swarming Granular Nematic'. In: *Science* 317.5834 (2007), pp. 105–108. ISSN: 0036-8075. DOI: 10.1126/science.1140414. URL: https://science.sciencemag.org/content/317/5834/105.

[41] R. Kemkemer, D. Kling, D. Kaufmann et al. 'Elastic properties of nematoid arrangements formed by amoeboid cells'. In: *Eur. Phys. J. E* 1 (2000), pp. 215–225. DOI: 10.1007/s101890050024. URL: https://doi.org/10.1007/s101890050024.

[42] O. Pohl and H. Stark. 'Dynamic Clustering and Chemotactic Collapse of Self-Phoretic Active Particles'. In: *Phys. Rev. Lett.* 112 (2014), p. 238303. DOI: 10.1103/PhysRevLett.112.238303. URL: https://link.aps.org/doi/10.1103/PhysRevLett.112.238303.

[43]   L. Oswald, S. Grosser, D. M. Smith and J. A. Käs. 'Jamming transitions in cancer'. In: *J. Phys. D: Appl. Phys.* 50.48 (2017), p. 483001. DOI: 10.1088/1361-6463/aa8e83. URL: https://doi.org/10.1088%5C%2F1361-6463%5C%2Faa8e83.

[44]   S. Garcia, E. Hannezo, J. Elgeti, J.-F. Joanny, P. Silberzan and N. S. Gov. 'Physics of active jamming during collective cellular motion in a monolayer'. In: *Proc. Natl. Acad. Sci. U.S.A.* 112.50 (2015), pp. 15314–15319. ISSN: 0027-8424. DOI: 10.1073/pnas.1510973112. URL: https://www.pnas.org/content/112/50/15314.

[45]   B. Ezhilan and D. Saintillan. 'Transport of a dilute active suspension in pressure-driven channel flow'. In: *J. Fluid Mech.* 777 (2015), pp. 482–522. DOI: 10.1017/jfm.2015.372. URL: https://doi.org/10.1017/jfm.2015.372.

[46]   C. F. Lee. 'Active particles under confinement: aggregation at the wall and gradient formation inside a channel'. In: *New J. Phys.* 15.5 (2013), p. 055007. ISSN: 1367-2630. DOI: 10.1088/1367-2630/15/5/055007. URL: http://dx.doi.org/10.1088/1367-2630/15/5/055007.

[47]   H. H. Wensink and H. Löwen. 'Aggregation of self-propelled colloidal rods near confining walls'. In: *Phys. Rev. E* 78 (2008), p. 031409. DOI: 10.1103/PhysRevE.78.031409. URL: https://www.researchgate.net/publication/23315634_Aggregation_of_self-propelled_colloidal_rods_near_confining_walls.

[48]   S. Henkes, Y. Fily and M. C. Marchetti. 'Active jamming: Self-propelled soft particles at high density'. In: *Phys. Rev. E* 84 (2011), p. 040301. DOI: 10.1103/PhysRevE.84.040301. URL: https://link.aps.org/doi/10.1103/PhysRevE.84.040301.

[49]   I. D. Vladescu, E. J. Marsden, J. Schwarz-Linek, V. A. Martinez, J. Arlt, A. N. Morozov, D. Marenduzzo, M. E. Cates and W. C. K. Poon. 'Filling an Emulsion Drop with Motile Bacteria'. In: *Phys. Rev. Lett.* 113 (2014). ISSN: 1079-7114. DOI: 10.1103/physrevlett.113.268101. URL: http://dx.doi.org/10.1103/PhysRevLett.113.268101.

[50]   L. Li, S. F. Nørrelykke and E. C. Cox. 'Persistent Cell Motion in the Absence of External Signals: A Search Strategy for Eukaryotic Cells'. In: *PLoS ONE* 3.5 (2008), e2093. ISSN: 1932-6203. DOI: 10.1371/journal.pone.0002093. URL: http://dx.doi.org/10.1371/journal.pone.0002093.

[51]   J. Elgeti and G. Gompper. 'Self-Propelled Rods near Surfaces'. In: *Eur. Phys. Lett.* 85 (2009), p. 38002. DOI: 10.1209/0295-5075/85/38002. URL: https://www.researchgate.net/publication/231030217_Self-Propelled_Rods_near_Surfaces.

[52] H. H. Wensink, J. Dunkel, S. Heidenreich, K. Drescher, R. E. Goldstein, H. Löwen and J. M. Yeomans. 'Meso-scale turbulence in living fluids'. In: *Proc. Natl. Acad. Sci. U.S.A* 109.36 (2012), pp. 14308–14313. ISSN: 1091-6490. DOI: 10.1073/pnas.1202032109. URL: http://dx.doi.org/10.1073/pnas.1202032109.

[53] M. Wilczek, D. G. Vlaykov and C. C. Lalescu. 'Emergence of Non-Gaussianity in Turbulence'. In: *Örlü R., Talamelli A., Oberlack M., Peinke J. (eds) Progress in Turbulence VII. Springer Proceedings in Physics* 196 (2017). DOI: 10.1007/978-3-319-57934-4_1. URL: https://doi.org/10.1007/978-3-319-57934-4_1.

[54] M. Dobson, I. Fox and A. Saracino. 'Cell list algorithms for nonequilibrium molecular dynamics'. In: *J. Comp. Phys.* 315 (2016), pp. 211–220. ISSN: 0021-9991. DOI: 10.1016/j.jcp.2016.03.056. URL: https://www.sciencedirect.com/science/article/pii/S0021999116300213.

Appendix A

Method Details

A.1 Optimization: Cell list algorithm

In particle model simulations with exclusively short-range interactions, a significant amount of computation resources can be saved from limiting the number of operations needed to compute the forces acting on any single particle. For a system of N particles, a naive implementation requires that for every particle whose data is updated, we compare its position to $N-1$ other particles. This results in a numerical complexity $\mathcal{O}(N^2)$. One relatively easily work-around is the use of a *cell list*, where the simulation domain is subdivided into smaller regions, each containing an associated list of the particles within the cell. At each system update, the particles are assigned to a list based on its current position, and forces are computed within each cell and the closest neighboring cells [54]. The size of each cell is chosen to be equal to or larger than the maximum range of the particle interactions. In this way, no non-zero forces are being neglected, while the number of position comparisons for each particle reduces to the order $\mathcal{O}(1)$. Because the number of particles contained in neighboring cells is independent of the total system size N, the process of calculating the short-range interactions reduces from $\mathcal{O}(N^2)$ to $\mathcal{O}(N)$, allowing for easier scalability with increased system sizes.

From testing the algorithm in conjunction with OpenMP-parallelization, using a cell list algorithm made a negligible difference in speeds for particle numbers $2000 < N < 4000$, and slightly increasing run time for $N < 2000$. This is probably due to a relatively large overhead created when assigning each particle to a cell list for each update of the system. The time used to perform these operations thus approximate the time saved. In addition, the method of parallelization was implemented differently, as each of the T processing threads was assigned a certain number of cells instead of a N/T portion of the N particle indices. The efficiency of the parallelization method seems to be affected by how well N/T approximates a whole number, as distributing the remainder of the division leads to additional overhead and idle threads. The cell list algorithm was therefore not used in the final simulations due to the negligible benefit with system sizes $N \sim 2000$.

A.2 System preparation

A.2.1 Initializing dense systems

The initial configurations for our systems of ABRs were constructed from running a simulation of N particles initially placed in a regular lattice configuration with randomly picked orientation $\mathbf{e}_i \in \{\hat{\mathbf{y}}, -\hat{\mathbf{y}}\}$, a method previously used in studies of active rods [27]. This method allows us to generate systems of high number densities compared to placing the particles with random positions and orientations, as we approximate a perfectly ordered close packing of 2D spherocylinders. Other methods include isotropic compression, whereby we initiate a dilute system with random positions and velocities and subsequently compress the system by either increasing the size of the particles or decrease the effective size of the system. This is done in an alternating process of compression and system relaxation until a satisfactory density is reached.

Before we start to gather data from the system, we would like to ensure that the system is minimally dependent on the initial regular grid. To find a suitable relaxation time for the systems, we simulate three random configurations for a selection of particle aspect ratios and typical parameter values and monitor the polar and nematic order parameters Π and ν. The dimensionless polar order parameter Π is defined as

$$\Pi = \frac{1}{N} \left| \sum_{i=1}^{N} \mathbf{e}_i \right|. \tag{A.1}$$

This is equivalent to the average system velocity used in the discussion of the Vicsek model. The nematic order parameter, describing the degree of global nematic ($\mathbf{n} = -\mathbf{n}$) order,

$$\nu = \frac{1}{N} \left[\left(\sum_{i=1}^{N} \cos(2\theta_i) \right)^2 + \left(\sum_{i=1}^{N} \sin(2\theta_i) \right)^2 \right]^{1/2} \tag{A.2}$$

The systems for $A = 4$ and $A = 10$ are allowed to evolve for a time interval $t = 100\tau$ and $t = 500\tau$, respectively. The measured polar and nematic order parameters are shown in Figure A.1. Representative snapshots from the pre-prepared regular configurations and finished states used for simulations are shown in Figure A.2, as well as zoomed-in views of the same systems in Figure A.3.

A.2.2 Discussion

As seen in Section 2.3, whenever particles interact via polar alignment interactions and are subject to subcritical noise levels, we expect to observe a sharp increase in global polar order in time. In simulations of ABRs, the interactions are apolar, but from Figure A.1, we still see a slight increase from the initial state with $\Pi \sim 0$. This is due to the spontaneous formation of polar clusters which aggregate rods of similar orientations. These clusters are visible in Figure A.2(b,d), indicated by

(a) $A = 4$, $\phi = 0.73$ **(b)** $A = 10$, $\phi = 0.49$
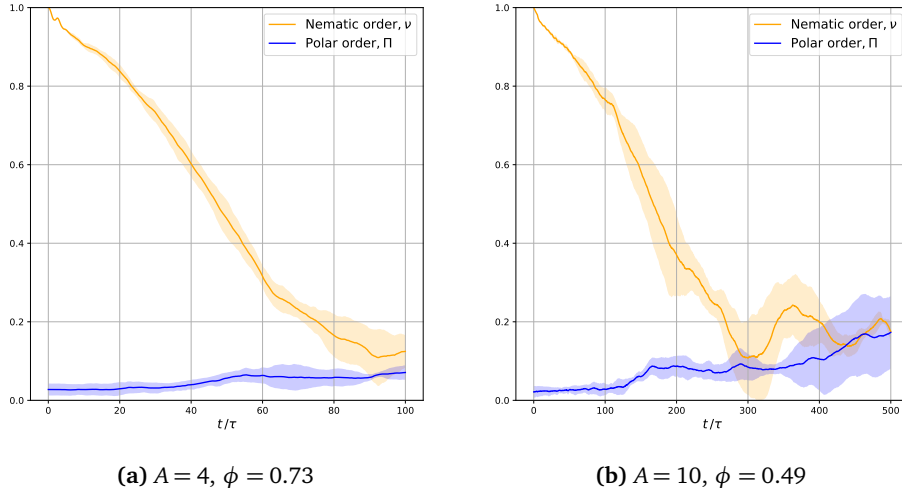
Figure A.1: *Transient order evolution*: Average order parameter measurements during preparation procedure. Shaded area shows standard deviation across three simulations. The systems seem to reach a steady state at longer times for rods with larger aspect ratios. $\beta = 0.1$, $Pe_r = 10^3$.

large regions of similarly colored rods. For the low noise levels used in these simulations, this aggregation will likely continue until most of the rods are aligned, similar to the Vicsek particles. This is allowed by the periodic boundary conditions which possess global translation modes. For shorter particles, the clusters seem to be smaller and more numerous, leading to high local polar order but a relatively weak global polar order. When the clusters collide, the expected behavior is similar to individual particles. Collision at a small relative angle creates a new combined region with the average orientation of the old regions, while larger angles reflect or split the regions. When constrained by the high density, however, the clusters are instead jammed.

Due to the nematic interaction, we also observe particles trapped within clusters of opposite polarity, locked in place by the surrounding rods. These occurrences halt the increase in polar order, but have no impact on the global nematic order. Due to the differing cluster sizes, this effect is more prominent in systems of longer rods. The onset of an apparent equilibrium in the nematic order parameter of the systems at $t \sim 100\tau$ for $A = 4$ and $t \sim 300\tau$ for $A = 10$ indicate that these are likely satisfactory values to reach a steady state with periodic boundary conditions, given a low noise regime.

(a) $A = 4$, $\phi = 0.73$, $t = 0$

(b) $A = 4$, $t = 100\tau$

(c) $A = 10$, $\phi = 0.49$, $t = 0$

(d) $A = 10$, $t = 500\tau$
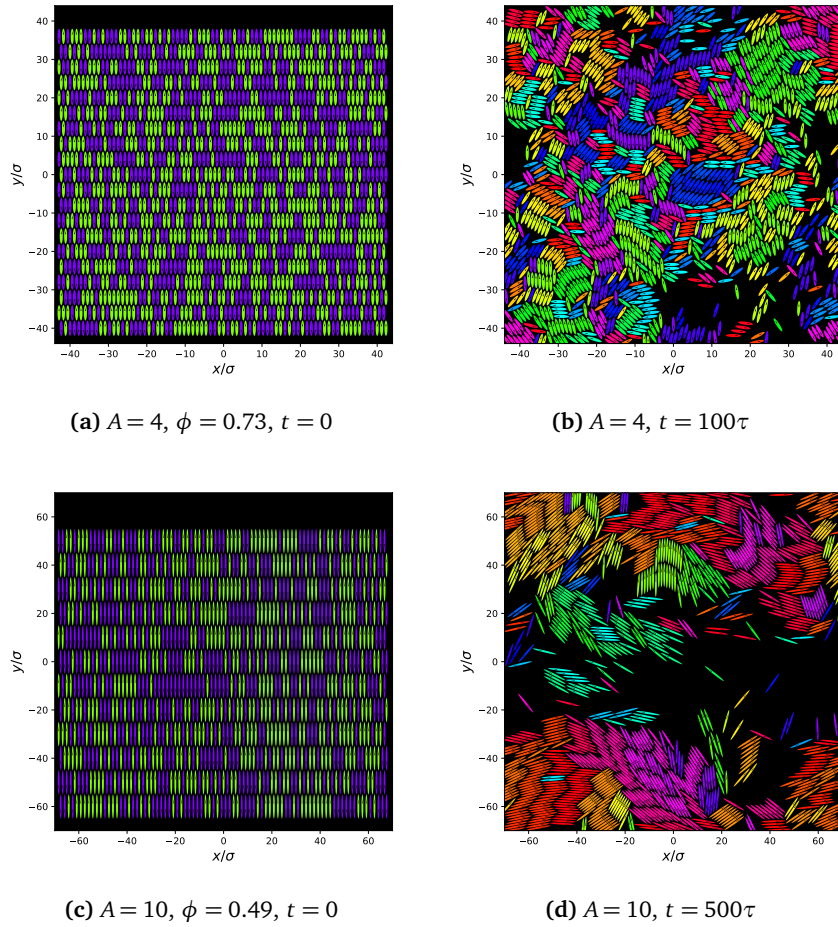
Figure A.2: *Dense system preparation*: Snapshots of $N = 1200$ rods from the initial regular grid configuration **(a, c)** and the configuration after some time when the system is allowed to evolve **(b, d)**. $\text{Pe}_r = 10^3$, $\beta = 0.01$.

(a) Closeup of initial grid for $A = 4$.

(b) Closeup of $A = 10$ rods, $t = 500\tau$.
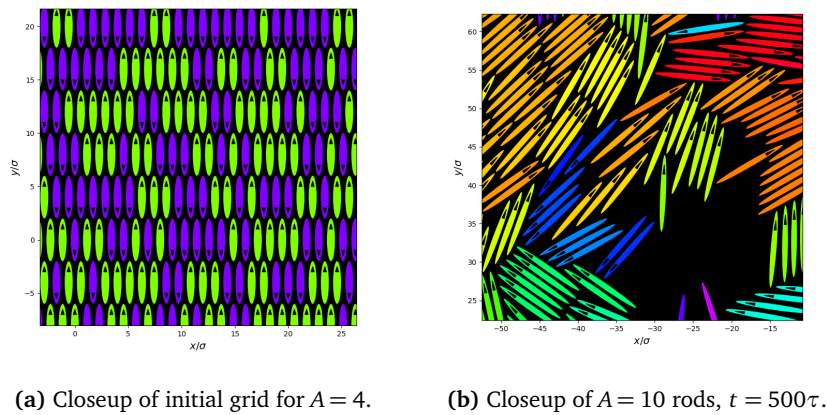
Figure A.3: *System preparation details*: Closeups from Figure A.2.